An in-depth numerical analysis of transient flow field in a Francis turbine during shutdown

Renewable Energy 179 (2021) 2322–2347

Contents lists available at ScienceDirect

Renewable Energy

journal homepage: www.elsevier.com/locate/renene

An in-depth numerical analysis of transient flow field in a Francis turbine during shutdown

Saeed Salehi [a, *], Håkan Nilsson [a], Eric Lillberg [b], Nicolas Edh [c]

[a] Division of Fluid Dynamics, Department of Mechanics and Maritime Sciences, Chalmers University of Technology, Gothenburg, SE-412 96, Sweden
[b] Vattenfall AB, Research and Development, SE-169 92, Solna, Sweden
[c] Forsmarks Kraftgrupp AB, 742 03, Östhammar, Sweden

ARTICLE INFO

Article history:
Received 26 December 2020
Received in revised form
26 June 2021
Accepted 23 July 2021
Available online 30 July 2021

Keywords:
Francis turbine
Transient operation
Shutdown sequence
Rotating vortex rope (RVR)
Deterministic and stochastic frequencies
OpenFOAM

ABSTRACT

Power production from intermittent renewable energy resources, such as solar and wind, has increased in the past few decades, leading researchers and engineers to establish techniques to preserve a stable electrical grid. Consequently, hydraulic turbines are being used more frequently in transient operating modes to regulate the grid. The present work provides a comprehensive numerical study on the transient flow field of a high-head Francis turbine model throughout the shutdown sequence. The computations were performed using OpenFOAM, utilizing the SST-SAS turbulence model. A Laplacian smoothing scheme is employed to conduct the mesh deformation of the guide vane domain. The time-averaged draft tube velocity field at the steady Best Efficiency Point (BEP) is validated against experimental data. Then different aspects of the transient flow field in the shutdown sequence are carefully assessed and explained for the first time. Short-Time Fourier Transform (STFT) analysis is carried out on the fluctuating part of the static pressure and force signals. High-amplitude low-frequency oscillations, due to the formation of a Rotating Vortex Rope (RVR) were observed during a specific period of the shutdown sequence. Thereafter, at deep part load conditions, the RVR vanishes and, a wide range of stochastic frequencies are identified at minimum load. A signal coherence analysis was accomplished to distinguish the deterministic and stochastic frequencies. The variation of the velocity field in the draft tube is described in detail with the help of velocity triangles. An in-depth explanation of the formation and variation of vortical structures during the whole sequence is presented. The physical mechanism of formation and destruction of the RVR is thoroughly explained.

1. Introduction

In recent years, global energy consumption has been increasing annually by 1.5% [1]. Electrical energy production from renewable energy resources, such as hydro, solar, wind, and biomass, has been growing fast to fulfill the current energy demand, owing to their availability and environmental friendliness. In fact, in 2019, renewable energy continued its record-breaking growth with a 200 GW capacity increase [2].

Electrical energy resources like solar and wind are intermittent since the generated power depends on the availability of sunlight and wind [3]. The electric power demand, on the other hand, does not vary as the availability of those resources, and the electric grid must therefore be regulated by controllable sources of energy [4,5]. Hydropower systems can store energy until it is needed and can be used to provide the required flexibility to balance the electrical grid at a wide range of time scales [6,7].

The operation of hydraulic turbines can be classified into two categories, namely, steady and transient modes. In steady mode, the rotational speed, guide vane angle, and flow rate of the turbine are preserved at a constant level, whereas one or more of these vary with time in transient modes. Most hydraulic turbines are designed to run at a steady Best Efficiency Point (BEP). Nonetheless, due to the need for regulating power, they are being used more frequently in transient operating modes. In fact, the flexibility and fast responsiveness of the hydropower systems make them a reliable solution to balance the electrical grid. Transient operation deteriorates the machines, due to unsteady and cyclic pressure loading [8]. Francis turbines are designed to have 1–10 start-stop

* Corresponding author.
E-mail addresses: saeed.salehi@chalmers.se (S. Salehi), hakan.nilsson@chalmers.se (H. Nilsson), eric.lillberg@vattenfall.com (E. Lillberg), nicolas.edh@vattenfall.com (N. Edh).

https://doi.org/10.1016/j.renene.2021.07.107

cycles each year [9]. It is estimated that traditionally in North America, the hydraulic turbines were allowed to go up to a maximum of 100 start-stops cycles per year, while the new power production tendency may require up to 500 cycles [10]. Therefore, future designs and refurbishments of hydraulic turbines must take transient operations over a wide range of operating conditions into account. A profound understanding of the flow during transients is thus essential. However, the complex flow instabilities that happen throughout the transient operations are not yet well understood. Accordingly, studies of the turbulent flow field in hydroturbines during transient operation are very important for the design of the next generation of hydropower systems.

Francis turbines can operate at a wide range of heads and flow rates and are thus being used in 60% of the hydropower plants in the world [3]. The Francis turbines may be operated in several different transients, namely, load variation (rejection or acceptance), start-stop (normal and emergency shutdown), and total load rejection [8]. Due to the need to increase the transient operation of Francis turbines, several experimental and numerical investigations have been performed in the past few years.

Nicolet [11] carried out hydroacoustic modeling of a Francis turbine power plant during transient operation. The dynamic behavior of the whole system was studied as well as different aspects of such transient conditions, e.g., pressure fluctuations, pressure and power surge, and rotor-stator interaction (RSI). It was shown that significant pressure fluctuations may occur in the whole system in the course of a fast load variation.

In a study by Trivedi et al. [12], six different transients (three load acceptance and three load rejection) were studied experimentally on a high-head Francis turbine. It was revealed that the speed of the guide vanes angle variation has a great impact on the pressure fluctuations and that an optimal speed could reduce the undesired fluctuations. The development of vortical flow structures in the vaneless space between the guide vanes and runner blades was observed by a Short-Time Fourier Transform (STFT) of the pressure fluctuations. Goyal et al. [13] performed experimental studies on the same high-head Francis turbine during load rejection, i.e. BEP to Part Load (PL). Particle Image Velocimetry (PIV) measurements were carried out in the draft tube to explain the physical mechanism behind the formation of the Rotating Vortex Rope (RVR). In addition, large pressure fluctuations due to both RSI and RVR were captured in the vaneless space and draft tube. Sotoudeh et al. [14] performed a numerical study on the same case and condition to further assess the formation of the RVR throughout the load rejection procedure. Recently, a novel numerical framework in OpenFOAM for simulation of Kaplan turbine transients was introduced by Salehi et al. [15].

Gagnon et al. [16] predicted the fatigue-based lifetime of a Francis turbine and showed that the startup scheme significantly influences the lifetime and reliability of the runner. The guide vane opening scheme and air admission were later shown to have a remarkable effect on the lifetime of the machine components [17]. An experimental investigation of a Francis turbine during shutdown and startup indicated that a faster transient procedure increases the pressure fluctuations notably [18]. Pressure measurements during the shutdown sequence of a model Francis turbine revealed that closing down the guide vanes completely before decoupling from the generator reduces the pressure fluctuation amplitude [19].

More recently, the startup sequence of a prototype Francis turbine was examined both experimentally and numerically [20]. It was shown that fatigue damage could be reduced by modifying the startup scheme. Counter-rotating vortex structures were observed in the simulations that produced high amplitude pressure pulsations.

Although experimental measurements can provide some information on the flow field of the turbines during different transient procedures, constructing an accurate experimental setup is highly expensive. In addition, many details of the complex flow instabilities during such operation cannot be easily measured or visualized. Therefore, establishing reliable numerical frameworks to accurately study and deeply understand the unsteady turbulent flow field throughout turbine transient operation is indispensable. However, trustworthy numerical simulations of the startup and shutdown sequences of hydraulic turbines are quite challenging. The total flow time is considerably long, and consequently, the computational cost is significantly high. The change of guide vane angles requires a formidable mesh deformation process, especially at deep part load when the guide vane opening angle is small. Hence, only a few researchers have employed Computational Fluid Dynamics (CFD) to study the hydraulic turbine startup sequence [20,21].

Some other research studies have been reported on the CFD simulation of shutdown sequence in pump-turbine [22–24] and axial turbine [25]. Mössinger et al. [26] and Salehi et al. [27] conducted CFD validation studies on the shutdown operation of a Francis turbine. However, to the best of the authors' knowledge, no comprehensive CFD study on details of the transient flow field of the Francis turbines during the shutdown sequence has been reported previously. Performing such research studies is essential to understand and untimely mitigate the damaging consequences of shutdown sequences that hydraulic turbines experience more frequently nowadays.

The purpose of the present paper is to provide an in-depth analysis of the transient turbulent flow field of a high-head Francis turbine model during a shutdown sequence. The numerical investigation is carried out using the OpenFOAM open-source CFD code and validated against experimental data at the steady BEP. Many aspects and features of a Francis turbine flow field during the shutdown are examined and described for the first time in this study, such as the time-variation of different high and low frequencies related to pressure and force pulsations, coherence analysis of fluctuations, as well as temporal variation of the velocity field. The λ_2-criterion is employed to visualize and explain the draft tube vortical structures (such as the RVR). Subsequently, the physical mechanisms of formation and collapse of such structures during the shutdown are thoroughly explained.

The rest of the paper is arranged as follows. Section 2 introduces the geometrical and operational details of the investigated test case. Section 3 provides a detailed description of the employed numerical framework, including mathematical formulations, numerical aspects of the CFD simulation, computational domain, and employed methodology for mesh deformation. The results are presented and discussed in Section 4. Finally, a summary of the paper and its concluding remarks are provided in Section 5.

2. Description of investigated model

2.1. Test case

In the present study, a high-head Francis turbine model known as Francis-99 is used as the investigated test case. The Francis-99 model turbine is a 1:5.1 scale model of a prototype Francis turbine located at Tokke power plant, Norway [28]. The model is provided by the Francis-99 workshop series [29] as a test case with experimental data to assess different numerical approaches. Fig. 1 presents a three-dimensional view of the model assembly, which consists of four domains: spiral casing, guide vanes, runner, and draft tube. The spiral casing contains 14 stay vanes, and the guide vane domain has 28 blades. The runner has 15 splitter blades and 15

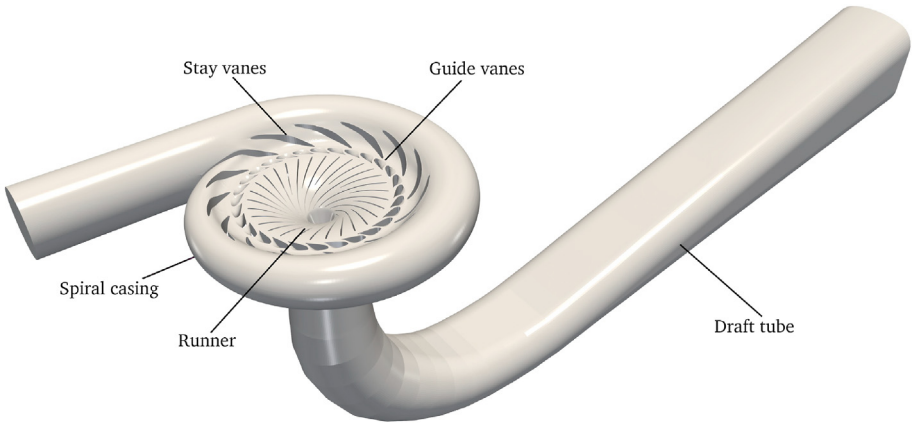

Fig. 1. Francis-99 model turbine assembly.

full-length blades. The inlet and outlet diameters of the runner are $D_{in} = 0.63$ m and $D_{out} = 0.347$ m, respectively. The prototype and model net heads, calculated as

$$H = p_{0,1} - p_{0,2} = \frac{p_1 - p_2}{\rho g} + \frac{v_1^2 - v_2^2}{2g} + z_1 - z_2, \quad (1)$$

are at the best efficiency point about $H_{prototype} \approx 377$ m and $H_{model} \approx 12$ m. In Eq. (1), indices 1 and 2 represent the spiral casing inlet and the draft tube outlet, respectively.

2.2. Available experimental data

During the Francis-99 workshops, a number of measurement locations were determined to compare data between numerical and experimental studies. Fig. 2 displays two cross-sections of the Francis-99 model, namely *y*-normal and *z*-normal. A PIV plane was established in the conical part of the draft tube, in which two in-plane velocity components were measured. The PIV plane is shown as a red line in the *z*-normal section (Fig. 2a) and a gray area in the *y*-normal section (Fig. 2b). The velocity components were reported along three lines of the PIV plane, which are illustrated in Fig. 2b. Lines 1 and 2 are horizontal, while Line 3 is axial along the draft tube center.

In addition, three locations were chosen for pressure measurements, as shown in Fig. 2b. The VL2 pressure sensor is located in the vaneless space between the guide vanes and the runner, measuring the strong pressure pulsations due to the rotor-stator interaction, while the DT5 and DT6 sensors measure the draft tube pressure. The draft tube sensors are piezoelectric type and only measure pressure fluctuations.

2.3. Operating conditions

The Francis-99 experimental data is available under various steady operating conditions, namely, Best Efficiency Point (BEP), Part Load (PL), and High Load (HL). Also, some transient operation sequences are available, i.e., load acceptance (BEP to HL), load rejection (BEP to PL), shutdown, and startup. The guide vane angle, α, which is measured relative to the completely closed position, changes between 0.80° and 12.43°, corresponding to minimum load and high load, respectively. The present study is focused on the shutdown procedure, as it is more challenging and complex in terms of both numerical simulations and fluid flow physics.

The turbine shutdown procedure initiates from the BEP operating condition. The guide vanes start to rotate (close) around their individual axes, and the flow rate consequently decreases. The guide vane angle and flow rate change linearly in time from $\alpha = 9.84°$ and $Q = 0.19959$ m^3/s at BEP to $\alpha = 0.8°$ and $Q = 0.022$ m^3/s at minimum load condition. During the whole sequence, the runner is rotating at a constant rotational speed of $\omega = 332.59$ rpm.

3. Numerical framework

The details of governing equations and computational aspects of the numerical framework are explained in this section.

3.1. Mathematical formulation

For a transient incompressible turbulent flow, the Reynolds-averaged equations of mass and momentum (also known as Unsteady Reynolds-Averaged Navier-Stokes, or URANS) are written in tensorial form as

$$\frac{\partial U_j}{\partial x_j} = 0, \quad (2)$$

$$\frac{\partial U_i}{\partial t} + \frac{\partial (U_i U_j)}{\partial x_j} = -\frac{1}{\rho}\frac{\partial p}{\partial x_i} + \frac{\partial}{\partial x_j}\left(\nu \frac{\partial U_i}{\partial x_j} - \overline{u_i\, u_j}\right), \quad (3)$$

where $-\rho \overline{u_i\, u_j}$ is the unknown Reynolds stress tensor which needs a turbulence model closure. In the present work, the Reynolds stress tensor is obtained using the Boussinesq (eddy-viscosity) hypothesis

$$\overline{u_i\, u_j} = -\nu_t \left(\frac{\partial U_i}{\partial x_j} + \frac{\partial U_j}{\partial x_i}\right) + \frac{2}{3} k \delta_{ij}, \quad (4)$$

where ν_t and k are turbulent viscosity and turbulent kinetic energy, respectively. The Shear Stress Transport based Scale-Adaptive Simulation model (SST-SAS) [30,31] is employed for the calculation of turbulent viscosity, which is obtained through solution of the transport equations for turbulent kinetic energy (k) and specific rate of dissipation (ω). SST-SAS is a turbulence resolving URANS model, commonly used for the simulation of practical transient flows. The scale adaptiveness reduces the amount of RANS modelling to allow a resolution of the flow structures that can be resolved by the mesh resolution and time step. On a fine mesh with a short time step it has the potential to provide LES-type of results.

The formulation of the SST-SAS model differs from the $k - \omega$ SST

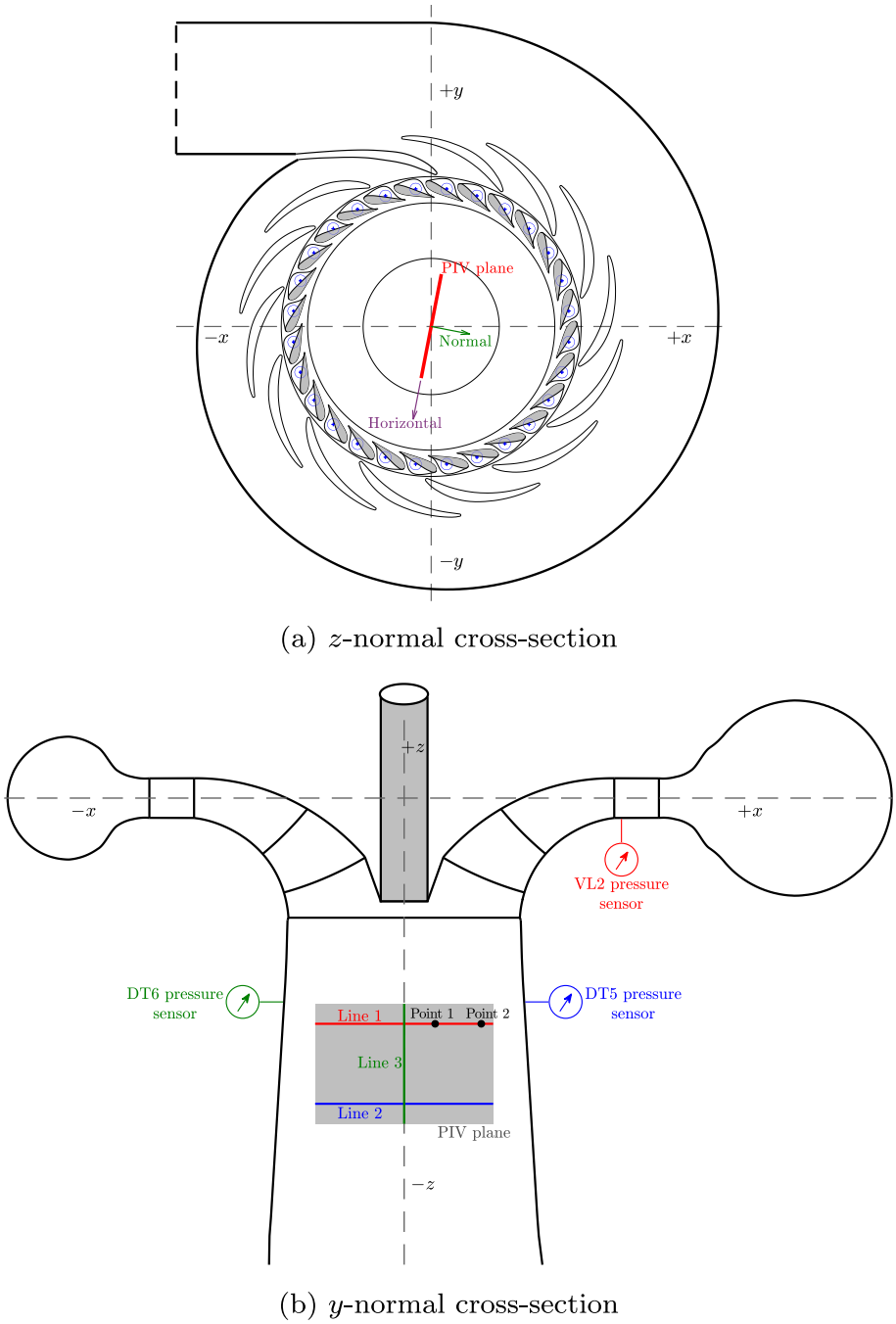

Fig. 2. Two cross-sections of the Francis-99 model, showing PIV plane, velocity lines, and pressure sensors.

RANS model [32] mostly by the introduction of an additional source term in the turbulence eddy frequency (ω) transport equation. This ω production term is defined as

$$Q_{SAS} = \max\left[\rho\zeta_2\kappa S^2\left(\frac{L}{L_{vK}}\right)^2 - C\frac{2\rho k}{\sigma_\Phi}\max\left(\frac{|\nabla\omega|^2}{\omega^2}, \frac{|\nabla k|^2}{k^2}\right), 0\right] \tag{5}$$

In the OpenFOAM implementation of the SST-SAS model, an upper limit of Q_{SAS} is also considered to guarantee numerical stability. The L_{vK} is the von Kármán length scale, defined by $\kappa|\boldsymbol{U}'/\boldsymbol{U}''|$, where $\boldsymbol{U}'$ and $\boldsymbol{U}''$ are first and second velocity spatial derivatives. Adding a lower constraint to ensure sufficient damping at the end of the turbulence spectrum, the L_{vK} length scale is defined as

$$L_{vK} = \max\left(\frac{\kappa S}{|\nabla^2\boldsymbol{U}|}, C_s\sqrt{\frac{\kappa\zeta_2}{\beta/c_\mu - \alpha}}\Delta\right) \tag{6}$$

Here the first velocity derivative $\boldsymbol{U}'$ is represented by $S = \sqrt{2S_{ij}S_{ij}}$ which is the scalar invariant of the strain tensor $S_{ij} = 0.5(\partial U_i/\partial x_j + \partial U_j/\partial x_i)$. The magnitude of the velocity Laplacian $|\nabla^2\boldsymbol{U}|$ represents the second velocity derivative. In addition, the lower limit of the L_{vK} in Eq. (6) is a factor of mesh cell size (Δ). In the present study the mesh cell size is calculated using the cube-root of cell volume delta.

The inclusion of this generalized von Kármán scale enables the model to adjust the local turbulent length scale based on L_{vK} and decreases the local eddy viscosity. Therefore, it can provide LES-like flow solutions and resolve the turbulent spectrum and break up of large eddies.

The SST-SAS model has been successfully applied to many industrial applications with unsteady turbulent flows [31,33–38]. More specifically, the model has been utilized and verified in the simulation of hydraulic turbine related flows [14,20,39–45].

3.2. Computational details

This section presents the computational framework and numerical aspects of the investigated problem, namely, CFD solver, discretization schemes, pressure-velocity coupling, boundary conditions, linear solvers, and parallel processing.

3.2.1. CFD solver

The CFD computations of the present study are performed using the finite-volume method on a collocated grid. The simulations are carried out with the OpenFOAM-v1912 software [46], which is a C++ object-oriented open-source CFD solver [47].

3.2.2. Discretization schemes

The general transport equation of the scalar φ over an arbitrary control volume V is as follows:

$$\underbrace{\frac{\partial}{\partial t}\int_V \varphi \,\mathrm{d}V}_{\text{temporal}} + \underbrace{\int_V \nabla\cdot\left(\vec{\mathrm{U}}\varphi\right)\mathrm{d}V}_{\text{divergence}} - \underbrace{\int_V \nabla\cdot(\Gamma\nabla\varphi)\,\mathrm{d}V}_{\text{Laplacian}} = \underbrace{\int_V S_\varphi \,\mathrm{d}V}_{\text{source}}, \tag{7}$$

where Γ is the diffusion coefficient and S_φ is the source term per unit volume. Each term in this equation should be separately discretized. The employed schemes to discretize these terms are explained and discussed in the current section.

3.2.2.1. Temporal schemes. Implicit time-marching is employed and all the temporal derivatives were discretized using the second-order backward scheme [48]. A fixed time step of $\Delta t = 1.25 \times 10^{-4}$ s was chosen for the transient simulations. The runner is rotating at a constant angular speed of 332.59 rpm. Consequently, the time step corresponds to 0.25° of runner rotation. The blade passing frequency is calculated as

$$f_\mathrm{b} = z_\mathrm{b} f_\mathrm{n}, \tag{8}$$

where z_b and f_n are the number of blades (main blades and splitters) and the rotational frequency of the runner, respectively. Therefore, for the current test case, the blade passing frequency is $f_\mathrm{b} = 166.3$ Hz, and the frequency of the solution time step is almost two orders of magnitude larger than the blade passing frequency. In other words, the chosen time step is small enough to resolve the most important flow structures and frequencies (e.g. runner blade frequency). In the shutdown sequence, the guide vanes are also changing their angle with a constant rotational speed of 1.3°/s. Hence the chosen time step corresponds to a guide vane rotation of 1.625×10^{-4} degrees.

The Courant-Friedrichs-Lewy (CFL) number [49] is monitored throughout the simulations to ensure numerical stability. The CFL number for one polyhedral cell is calculated in OpenFOAM as

$$\mathrm{CFL} = \frac{\Delta t}{2\mathcal{V}} \sum_{i\in \text{Cell faces}} |\Phi_i|, \tag{9}$$

where $\mathcal{V}$ is the cell volume and Φ_i represents the volumetric flux of face i, calculated as the inner product of velocity vector at the face center and the face normal vector. The mean and maximum CFL numbers at BEP are 0.025 and 55, respectively. It is worth mentioning that the CFL number is lower than 2 in 99.4% of the cells. In the shutdown sequence, the guide vanes close down, and the flow rate decreases. Hence the mean CFL number decreases throughout the whole sequence and stays at an almost constant value of 0.015 at the minimum load condition. The maximum CFL number first decreases to 27 due to the flow rate reduction. After 3 s into the transient sequence, the maximum CFL number increases to 121 in the guide vane region, due to the local mesh deformation and cell size reduction.

3.2.2.2. Gradient schemes. The gradient terms (for instance the pressure gradient source term) are generally discretized in OpenFOAM using the second-order central differencing scheme. If there are low-quality cells in the domain, which can happen in many practical cases due to geometrical complexity, the approximation of the gradient could be very large and cause numerical instability. In this paper, a limiter approach, known as *cellLimited*, is employed to provide boundedness and stability of the gradient terms. This limiting method ensures that the interpolated face values do not exceed the range of surrounding cell center values.

3.2.2.3. Divergence schemes. Using Gauss' theorem, the divergence term can be reformulated into a sum of the fluxes through the faces, as

$$\int_V \nabla\cdot(\vec{U}\varphi)\,\mathrm{d}V = \sum_f \vec{S}\cdot(\vec{U}\varphi)_\mathrm{f}, \tag{10}$$

where $\vec{S}$ is the face area normal vector and φ is the transported variable. In OpenFOAM, the face fluxes ($\vec{S}\cdot\vec{U}_\mathrm{f}$) are updated and stored as part of the solution process, while the transported variable at the face (φ_f) needs to be determined using an interpolation scheme. The Linear-Upwind Stabilised Transport (LUST) convection scheme [50] is used in the present work. It is an unbounded discretization scheme that blends the central and second-order upwind schemes (i,e., *linear* and *linearUpwind*). The central and second-order upwind schemes interpolates the face-centered values (φ_f) as

$$\varphi_{\mathrm{f,c}} = \lambda\varphi_\mathrm{u} + (1-\lambda)\varphi_\mathrm{d}, \quad \text{where} \quad \lambda = \frac{\boldsymbol{x}_\mathrm{d} - \boldsymbol{x}_\mathrm{f}}{\boldsymbol{x}_\mathrm{d} - \boldsymbol{x}_\mathrm{u}}, \tag{11}$$

and

$$\varphi_{\mathrm{f,lu}} = \varphi_\mathrm{u} + (\boldsymbol{x}_\mathrm{e} - \boldsymbol{x}_\mathrm{u})\cdot\nabla_\mathrm{u}\varphi, \tag{12}$$

respectively. Subscripts d, and u refer to downwind and upwind cells while f denotes the current face. $\nabla_\mathrm{u}\varphi$ is the cell center gradient at the upwind cell. The LUST scheme blends these two schemes using a weighted averaging

$$\varphi_{\mathrm{f,LUST}} = \gamma\varphi_{f,\mathrm{c}} + (1-\gamma)\varphi_{f,\mathrm{lu}}, \tag{13}$$

where blending factor γ is set to 0.75 in the present study. It means that the face values of the dependent variable are calculated by

blending 75% of the second-order central scheme and 25% of the second-order upwind scheme. The factor provides a compromise between accuracy and numerical stability. Although the scheme maintains a second-order accuracy, its stability is higher than the central scheme and it is much less diffusive than the second-order upwind scheme. The scheme can be a good choice for turbulence resolving simulation of engineering unsteady flows with complex meshes, where the pure central scheme can not be used due to numerical oscillations.

Here, the LUST scheme is applied for the three velocity components, while the second-order upwind scheme is used for k and ω.

3.2.2.4. Laplacian schemes. The Laplacian term can also be rewritten using Gauss' theorem, as

$$\int_V \nabla\cdot(\Gamma\nabla\varphi)\,\mathrm{d}V = \sum_{\mathrm{f}} \Gamma_{\mathrm{f}}\vec{S}\cdot(\nabla\varphi)_{\mathrm{f}}. \tag{14}$$

The central second-order scheme with explicit non-orthogonal correction is employed for the calculation of this term. Here again, because of numerical instabilities due to mesh quality in some regions, a limiter is utilized for the non-orthogonal correction part.

3.2.3. Pressure-velocity coupling

The pressure field is linked to the velocity field through the PIMPLE algorithm, which combines two pressure correction algorithms, namely, the Semi-Implicit Method for Pressure Linked Equations (SIMPLE) [51] and the Pressure Implicit with Split Operator (PISO) [52]. In each PIMPLE loop, the SIMPLE algorithm works as an outer loop while the PISO algorithm is used as an inner loop. If only one outer loop is performed, the PIMPLE algorithm operates as a pure PISO algorithm. Increasing the number of outer loops enables the use of longer time steps (Co $\gg$ 1) while preserving stability and time accuracy. More details on the PIMPLE algorithm and its flowchart are given by Robertson et al. [53] and Holzmann [54].

In the present work, a maximum of 10 outer loops is considered in each time step, unless a specified tolerance is reached and breaks the loop. The tolerance is a residual criterion, which is here set to 10^{-5} and 10^{-6} for p and U, respectively. In each outer loop, the two inner loops of the standard PISO algorithm are conducted. The non-orthogonality is high in some parts of the mesh, due to the complexity of the geometry. Therefore, in each inner loop, one additional non-orthogonal correction loop is carried out to ensure convergence of all explicit parts in the discretized equations. It is worth mentioning that all the above-mentioned settings in the PIMPLE solver were acquired after excessive numerical experiments to find the best options to ensure numerical stability, accuracy, and reasonable computational cost.

Special interpolation techniques should be used in the collocated approach to avoid unphysical pressure oscillations. Although the Rhie-Chow interpolation technique [55] is not explicitly implemented in OpenFOAM, it can be shown that the utilized pressure-velocity coupling algorithm resembles this interpolation technique [56].

Furthermore, the turbulence transport equations are solved only once at the end of the final outer loop. In this way, the turbulent viscosity (and subsequently turbulent Reynolds stress) is updated when the momentum equation is fully converged. This strategy provides a compromise between accuracy and computational cost.

The studied shutdown sequence of a Francis turbine involves the use of a dynamic mesh, due to both the solid-body rotation of the runner and the mesh deformation owing to the movement of the guide vanes. Therefore, in each time step, the mesh is updated at the beginning of the first PIMPLE outer loop (the mesh motion itself is described in Section 3.5). Subsequently, the face fluxes are calculated relative to the mesh motion to satisfy the mass conservation [57].

3.2.4. Boundary conditions

The boundary conditions during the shutdown process are to a great extent depending on the guide vane motion. The guide vanes change their angle (close down) with a constant rotational speed of 1.3°/s. Fig. 3a presents the variation of the guide vane angle throughout the whole simulation. Our experience is that a sudden sharp transition between the standstill and moving states of the guide vanes generates numerical instabilities and pressure surge effects. This is in accordance with previous investigations in the literature [26,58–60]. Hence, the starting and stopping processes of the guide vane rotation at $t = 1$ and $t = 8$ s are given a smooth transition using a 5th order polynomial (see the zoomed view in Fig. 3a). The employed smooth guide vane closure law is compared to the experimental data to show the consistency of the utilized boundary condition and the experiments.

The guide vane motion is implemented as a new boundary condition for the Laplacian mesh deformation in OpenFOAM. Each guide vane is given the rotational speed as well as its individual rotational axis. Having obtained a smooth curve for the guide vane angle, the rotational speed of the guide vanes is calculated simply by taking a time-derivative of the angle curve (Fig. 3b).

The experimentally measured discharge data in transient mode is not accurate enough, due to the response time of the utilized flow meter [29]. Following workshop proposition and previous studies in the literature, the turbine volume flow rate is assumed to vary linearly with respect to the guide vane angle [14,26,29,61]. A time-varying spatially uniform velocity is imposed to the inlet of the spiral casing, based on the smooth curve of guide vane angle presented in Fig. 3a. The inlet values of turbulent kinetic energy k and the specific rate of dissipation ω are also varying with time assuming a constant turbulence intensity ($I = 7\%$) and viscosity ratio ($\nu_t/\nu = 100$). The inlet pressure is based on a zero-gradient assumption. It should be mentioned that the inlet turbulence quantities did not have any considerable impact on the monitored results in the regions of interest and mostly affected the solution convergence. At the outlet boundary, the zero-gradient condition is imposed for U, k, and ω, while the pressure is assumed to be fixed. A special treatment is applied at the outlet boundary, which prevents backflow by setting the velocity to zero at faces where the flux tends to be reversed. The outlet boundary is far away from the region of interest and thus this numerical treatment does not have any effect on the monitored results.

A no-slip boundary condition is applied for the velocity at all walls, where the turbulent kinetic energy is set to a near-zero value. The turbulent specific dissipation rate and turbulent viscosity are also calculated using the *omegaWallFunction* and *nutUSpaldingWallFunction* wall functions which provide wall constraint conditions. The wall pressure is computed based on a zero-gradient assumption.

The mesh is divided into four domains, i.e., spiral casing, guide vanes, runner, and draft tube. The non-conformal mesh interfaces are coupled using the Cyclic Arbitrary Mesh Interface (*cyclicAMI*) boundary condition. This interface transfers the flow properties using a conservative interpolation based on an efficient strategy developed for general transport equations [62,63].

The shutdown sequence starts at BEP and goes to minimum load. To simulate the whole sequence accurately a fully developed flow at BEP should be first established. Therefore, a steady potential

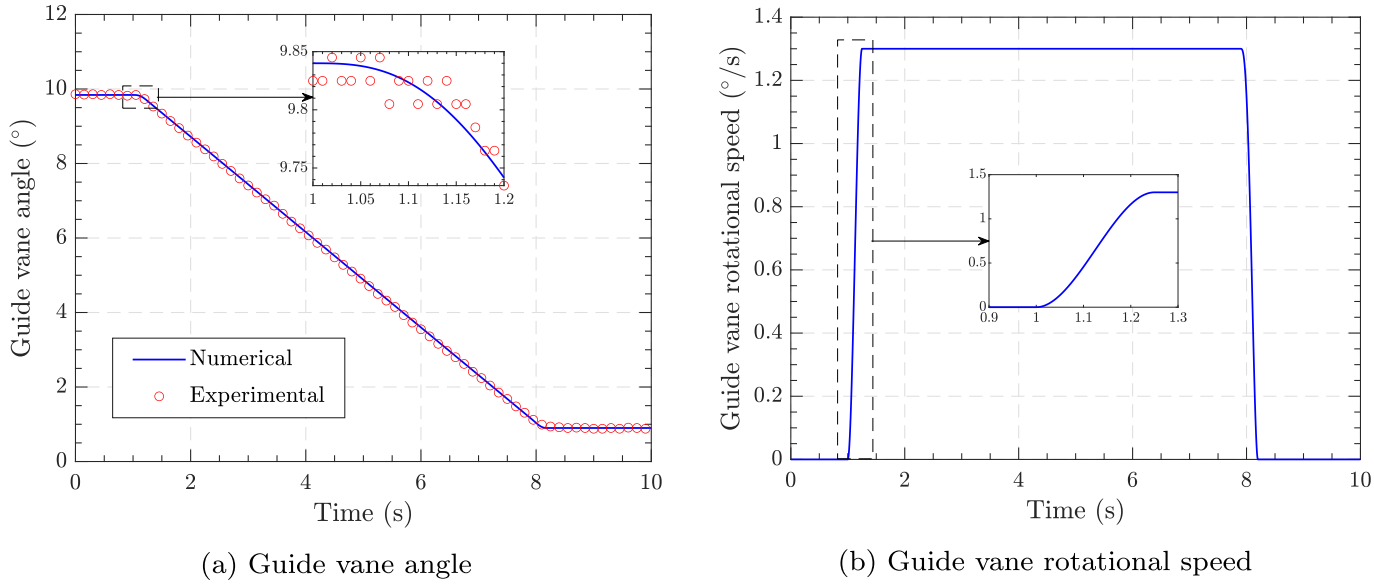

(a) Guide vane angle (b) Guide vane rotational speed

Fig. 3. Variation of (a) guide vane angle and (b) rotational speed for the shutdown process.

flow is first solved to give an initial guess, followed by an unsteady turbulent flow simulation until the flow is fully developed at BEP. Hence, the BEP flow is solved for 2 s flow time, corresponding to 11 runner rotations, which in our experience is more than enough to reach a fully developed flow. Several local and integrated flow properties were monitored to ensure the establishment of a statistically stationary state. Then the shutdown sequence presented in Fig. 3 starts. The whole transient simulation covers $t = 10$ s, corresponding to 55.43 runner revolutions.

3.2.5. Linear solvers

The discretizations of the transport equations result in linear systems that are solved by linear solvers. In the present work, the Geometric Agglomerated Algebraic Multi-Grid (*GAMG*) solver is employed to solve the pressure equation with the combined DIC and Gauss-Seidel smoother. The iterative *smoothSolver* with Gauss-Seidel smoother is used to solve the linear system of equations for the velocity, turbulent kinetic energy, and specific dissipation rate. The solution of dynamic mesh equations (described in Section 3.5) is also obtained using the *GAMG* solver, which showed better stability during our numerical experiments.

3.3. Parallel processing

The simulation is carried out using parallel processing on multiple cores. The scotch [64] decomposition method with uniform weights is utilized, ensuring load balance and minimizing the number of processor boundary interfaces. The inter-process information is exchanged using the Message Passing Interface (MPI) [65]. The job is submitted to 10 compute nodes of an HPC Linux cluster. Each compute node contains two Intel Xeon Gold 6130 CPUs with 16 cores each (32 cores on each node) and 96 GiB of RAM. Hence the parallel computation is performed using 320 cores. Each time step requires a wall-clock time of 15 s to complete. Consequently, the transient simulation of 12 s flow time takes around 400 h, or 17 days, to complete all the 96000 time steps. In other words, a computational cost of 128,000 core hours is required to complete one transient simulation.

3.4. Computational mesh

The full computational domain of the Francis-99 model turbine, i.e., from the inlet of the spiral casing to the outlet of the draft tube, is considered in this study. Hence, four domains, namely, spiral casing, guide vanes, runner, and draft tube constitute the present computational model (see Fig. 1). The corresponding mesh of each domain is generated separately. Block-structured meshes are generated in ICEM-CFD for the spiral casing, draft tube, and a two-blade (main and splitter blades) periodic section of the runner. A single periodic guide vane passage is meshed using Turbo-grid. The runner and guide vane O-grid meshes are then copied to cover all the blades over the entire 360°. The meshes of the four domains are then merged together in OpenFOAM, constructing the full computational domain.

At an early stage of this work, a mesh study was conducted to ensure the independence of the numerical results to the mesh resolution. Both integrated and local quantities at BEP were compared to experimental values. The minimum error in prediction of the runner torque (with respect to the experimental value) and draft tube velocity distribution corresponded to the finest mesh. The corresponding results are not presented here, due to brevity. Therefore, the finest mesh was chosen for the rest of the computations. Fig. 4a provides an overall view of the turbine assembly, while close-ups of the spiral casing mesh (around the stay vane trailing edges) and guide vane leading edges are shown in Fig. 4b and c, respectively. It should be noted that the guide vane mesh deforms during the simulation due to the change of angle of the guide vane and that Fig. 4c illustrates the guide vane mesh at BEP. Despite the bulges that are seen near the lower and upper surfaces of the guide vanes, they completely cut off the flow rate when they are fully closed. Zoomed views of the leading and trailing edges of the runner blades (main blades and splitters) are shown in Fig. 4d and e. The complete mesh assembly contains almost 16 million cells. The details of the mesh parameters are presented in Table 1, where also the maximum and average values of the y^+ value at the BEP and minimum load conditions are provided. The mean values of y^+ show that the viscous sub-layer is resolved in the draft tube, which is the main interest in the present work.

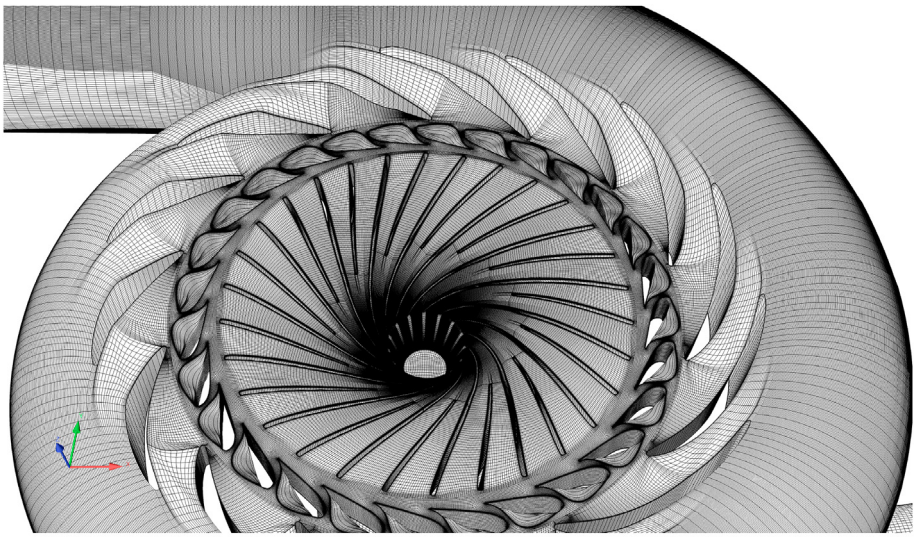

(a) Turbine assembly

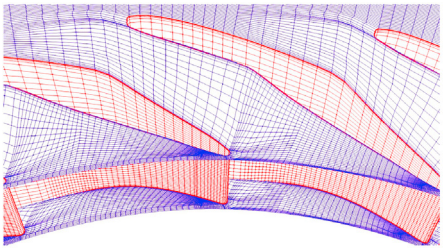

(b) Stay vanes

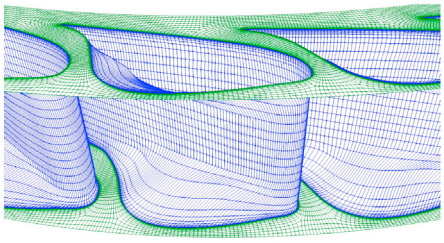

(c) Guide vanes

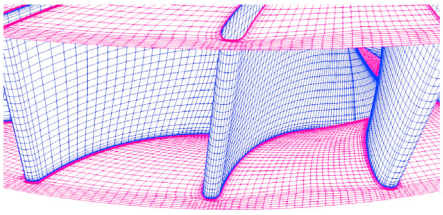

(d) Runner blade leading edges

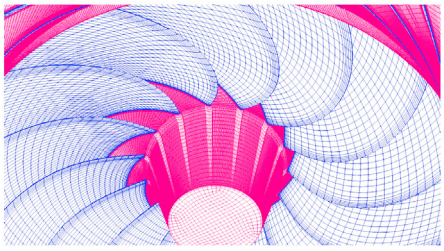

(e) Runner blade trailing edges

Fig. 4. Computational mesh at best efficiency point.

Table 1
Grid details parameters.

Domain	Number of cells	BEP		Minimum load	
		y^+_{max}	y^+_{mean}	y^+_{max}	y^+_{mean}
Spiral casing	5.57×10^6	45.33	13.47	8.02	2.76
Guide vane	2.66×10^6	13.85	8.45	17.39	5.15
Runner	5.47×10^6	9.81	3.88	8.82	2.07
Draft tube	2.27×10^6	2.10	1.01	3.04	1.04

3.5. Mesh motion strategy

In a Francis turbine working in a transient operating sequence, each guide vane rotates around its own individual axis, while the runner is also rotating at the same time. Hence, a numerical simulation of such flow involves mesh deformation due to guide vane movement at the same time as the runner mesh is rotating as a solid body. In order to carry out such simulation, an advanced dynamic mesh tool in OpenFOAM is utilized that allows employing different mesh motion strategies on different cell zones. Therefore, at each time step, a prescribed solid body rotation is applied in the runner domain, while a Laplacian mesh morphing solver is used for the mesh deformation of the guide vane domain. The spiral casing and draft tube meshes are static. As the mesh points are moved to their new locations, the mesh face fluxes are calculated and taken into account in the convection terms of the transport equations. More details on the dynamic mesh procedure in OpenFOAM, including mesh morphing, are described by Jasak and Tuković [66] and Jasak [67].

3.5.1. Laplacian displacement solver

The mesh morphing through Laplacian smoothing is in OpenFOAM governed by

$$\nabla \cdot (\mathcal{K} \nabla \boldsymbol{\delta}_{\text{cell}}) = \mathbf{0}, \tag{15}$$

where $\boldsymbol{\delta}_{\text{cell}}$ is the displacement vector of the cell centers. It should be noted that in order to calculate the location of the new points, one needs the displacement field of the points $\boldsymbol{\delta}_{\text{point}}$ (i.e., *pointDisplacement*). But OpenFOAM, as a cell-centered finite volume

solver, calculates the Laplacian equation for the cell-centered displacement (i.e., *cellDisplacement*) and then the solution is interpolated to the points to get the *pointDisplacement* field and consequently the location of the new points. The boundary conditions are imposed by the user for the *pointDisplacement* field, and automatically transferred by OpenFOAM to the *cellDisplacement* field. Therefore, the boundary condition presented in Fig. 3b is applied on the points of the guide vane boundary patches. Having obtained the solution for the displacement of the points, the location of new points are simply calculated as

$$\boldsymbol{x}^{t+1}_{\text{point}} = \boldsymbol{x}^{t}_{\text{point}} + \boldsymbol{\delta}^{t}_{\text{point}}. \tag{16}$$

In Eq. (15), $\mathcal{K}$ is the motion diffusivity, which spreads out the displacement imposed by the boundary to the interior of the mesh. The diffusivity may be specified as linear, exponential, inverse distance to the object, or via any arbitrary decreasing function. An inverse distance approach with respect to the guide vane blade surfaces is employed in the present work for diffusivity. This makes the points located close to the moving patch more affected by the boundary movement than those further away [68]. Consequently, the cells close to the moving guide vanes move almost as solid body, while the cells far away from the boundary deform considerably. The inverse distance diffusivity is shown in Fig. 5, at the mid-plane of the guide vane domain. Fig. 6 illustrates the unmorphed best efficiency point guide vane mesh ($\alpha = 9.84°$) as well as rotated guide vanes with morphed meshes at $\alpha = 7.40°$ and $\alpha = 5.20°$. It should be recalled that the guide vane angles are calculated with respect to a fully closed position.

Points on the inlet and outlet boundaries of the guide vane domain, where *cyclicAMI* condition is imposed, are kept fixed during the mesh morphing. On the other hand, points on the lower and upper surfaces of the guide vane domain are expected to slip on the surface. The general *slip* boundary condition in OpenFOAM works as an explicit correction after the solution is obtained in each time step. Our experiences in dynamic mesh handling in OpenFOAM show that this kind of correction is not stable and is very sensitive to small distortions which will accumulate and increase unless they are explicitly removed. Although, there are more stable alternatives in OpenFOAM that could be utilized for this case, such as *fixedNormalSlip* and *surfaceSlipDisplacement*, a new dynamic mesh library is implemented in OpenFOAM to tackle this problem and make sure that the points of the upper and lower surfaces slip on the actual geometric flat surface. In this approach, an extra correction step is added to the final stage of the dynamic mesh calculations. After obtaining the position of the new point positions at the slip boundaries, the point positions are corrected according to the mathematical descriptions of the upper and lower surfaces.

4. Results and discussion

4.1. Validation at best efficiency point

The initial 1 s of the studied transient is at the statistically stationary BEP condition (see Fig. 3). In Fig. 7 we validate the velocity profiles, time-averaged over this period, comparing it with the available experimental PIV data along the measurement lines (see Fig. 2). To repeat, the axial velocity (W) is aligned with the runner axis of rotation, with negative values in the main flow direction. The horizontal velocity (U) is perpendicular to the axial direction and aligned with the PIV plane. The normal component (V) is perpendicular to both the other components and normal to the PIV plane. The directions are also shown in Fig. 2.

The numerical and experimental results agree very well for both the horizontal and axial velocities. For the axial component, it can particularly be noted that the wake below the runner crown is captured the same in both simulation and experiment. This is the region with the largest differences in the previous numerical studies that can be found in the literature, which argues that the present results are of the highest possible accuracy. For the horizontal velocity, there is a slight shift between the experimental and numerical results. Approximating the numerical and experimental data at Lines 1 and 2 by straight lines, it can be seen that the numerical results are quite symmetric about the centerline (negative on one side and positive on the other side) while the experimental results are always negative. It should be noted that the horizontal velocity component is directly related to the radial component, with a shift in sign at the centerline. The numerical results suggest that there is a positive radial flow at both sides of the centerline, in accordance with the expansion of the draft tube. The wiggles at the center are connected to the recirculation region and are therefore difficult to explain in detail. They may be caused by a too short time for the time-averaging. It is those wiggles that give a deviation from zero along Line 3, for the numerical results. The experimental

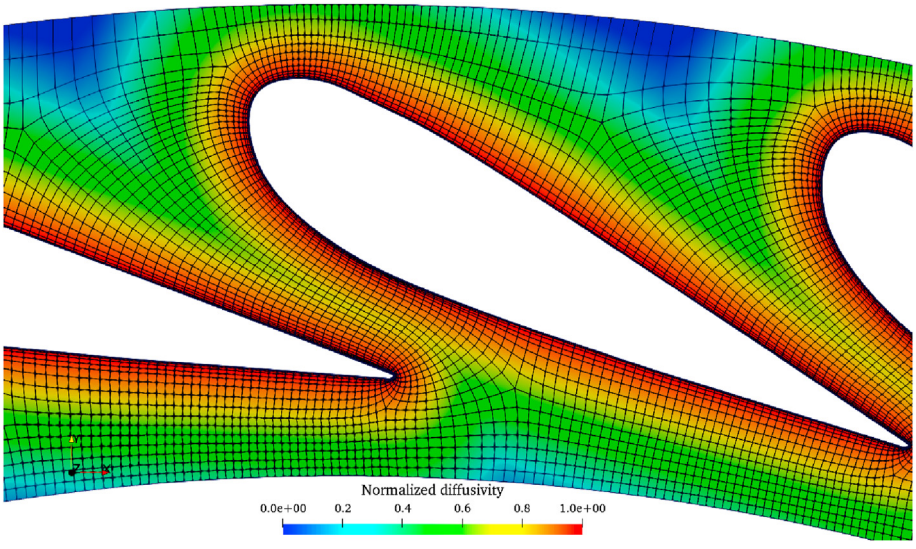

Fig. 5. Normalized inverse distance diffusivity with respect to guide vane blades, shown at the middle plane of the guide vane domain.

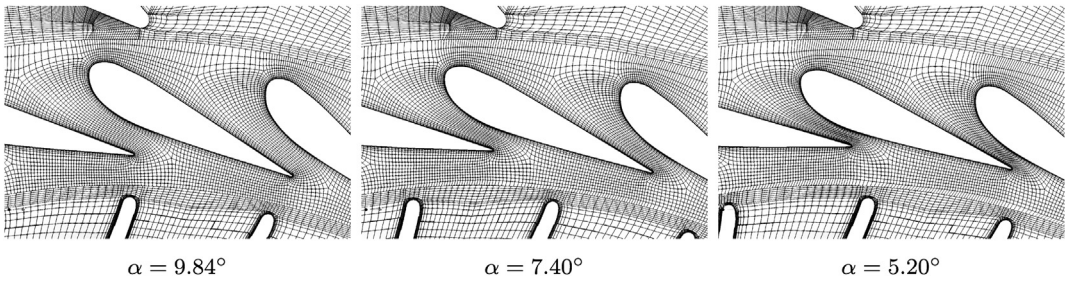

Fig. 6. Visualization of mesh morphing on the middle plane of the guide vane domain, where α is the guide vane blade angle computed with respect to the fully closed position.

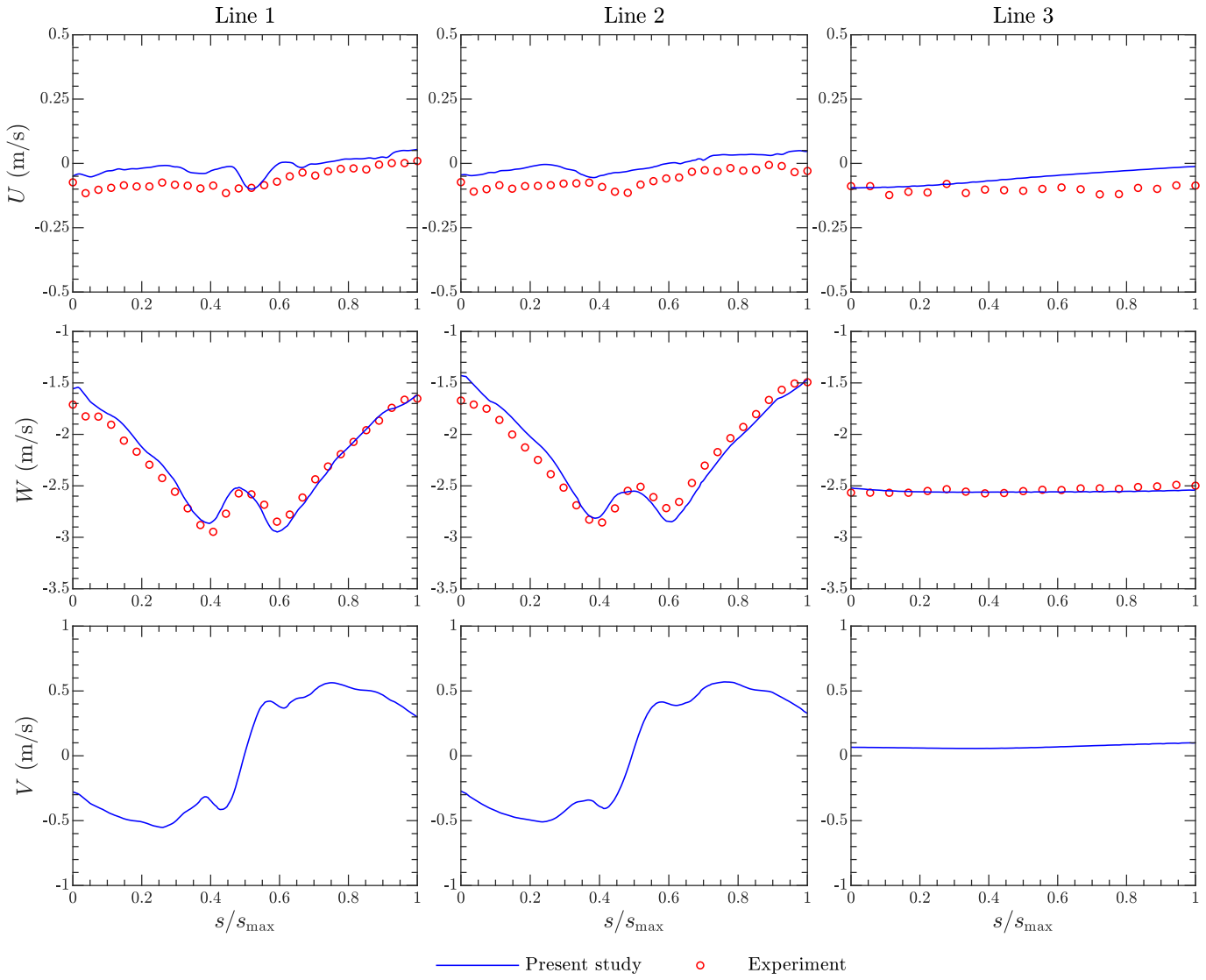

Fig. 7. Time-averaged results of horizontal (U), axial (W), and normal (V) velocities on different lines at BEP condition. Numerical results are compared to the experimental PIV data.

horizontal velocity suggests that the flow is in the positive radial direction on one side of the centerline and in the negative radial direction on the other side of the centerline. This may happen if the center of the vortex is not exactly in the PIV plane, either because the vortex is shifted or because the PIV plane is not perfectly centered. The vortex could be shifted due to some non-axisymmetry in the case, such as the spiral casing or draft tube bend. However, both of those effects are included in both the experimental and numerical studies. It should however be noted that the extraction of flow data at a vortex center is very sensitive and that the values are very small compared to those of the axial component. The direction of the V component changes near the center, showing the presence of a swirling flow at both Lines 1 and 2. A non-zero normal component is observed on Line 3, indicating that the draft tube vortex is slightly off-centered.

Global time-averaged data, such as the pressure at the VL2

sensor (which is relative to the outlet pressure, and thus relates to the losses in the system), shaft torque, net head, and hydraulic efficiency are validated against the experimental data in Table 2. The relative errors of all quantities are less than 2.1%, showing a good agreement.

Lacking possibilities to further investigate the details of the experimental data acquisition, we conclude that the experimental and numerical results are very similar and that the numerical results at BEP are valid.

4.2. Shutdown sequence

In this section, the transient results for the turbine shutdown sequence are presented and discussed, where the guide vane angle and flow rate change according to the prescribed time-varying boundary conditions explained in Section 3.2.4.

4.2.1. Static pressure variation

The unsteady static pressure is monitored at experimental sensor locations VL2, DT5, and DT6 (see Fig. 2) during the entire sequence shown in Fig. 3. It should be noted that in the experiments, the static pressure was measured at the VL2 location, while only static pressure fluctuations were measured at DT5 and DT6. In transient sequences like turbine shutdown or startup, the pressure signals consist of both a variation due to the change of operation and fluctuations due to rotor-stator interaction and flow instabilities. Therefore, one must employ a signal analysis method to obtain the instantaneous mean and the fluctuations with respect to that instantaneous mean. In the present study, the Savitzky-Golay finite impulse response filter [69] is utilized to smooth out the captured pressure signals and acquire the pressure instantaneous mean. A time window needs to be defined to calculate the smoothed data. The size of the window should be chosen in a way to capture all the pressure fluctuations. If the window is too small, only high-frequency perturbations are captured and low-frequency fluctuations (for instance fluctuations due to rotating vortex rope) will be missed. On the other hand, a too large window size results in accounting for some part of the pressure level variation due to the transient sequence as fluctuations. Especially at the start and end of the shutdown sequence, where the pressure variation is sharp. Therefore, a variable window size, which is smaller where the variation of pressure level is sharper, is utilized in this study to extract all the fluctuations. Having obtained the instantaneous mean ($\bar{p}$), the fluctuating part of the pressure can be simply calculated by

$$p' = p - \bar{p}. \tag{17}$$

The pressure data for the VL2 (vaneless space) and DT6 (draft tube) probes are displayed in Fig. 8. The numerical results and experimental data show a good agreement. The maximum relative error for the VL2 sensor is 4.9%, corresponding to the minimum load condition where the pressure is slightly over-predicted by the simulation. The zoomed view for the VL2 sensor in Fig. 8a covers a 90° rotation of the runner in the stationary BEP phase. Therefore, 7.5 pulsations due to the RSI are visible in this plot, showing that both the amplitude and frequency of the RSI pressure fluctuations are captured well. When the guide vane movement and flow rate reduction initiate at $t = 1$ s, the pressure starts decreasing with an almost constant rate. The instantaneous mean of the pressure in the vaneless space drops down from 174 kPa (at BEP) to 160 kPa (at minimum load). Low-frequency and high-amplitude fluctuations are observed from $t = 4$ s, which is due to the formation and breakup of large flow structures in the draft tube (i.e., RVR). The large fluctuations seem to diminish after $t = 6$ s. Then again, in the minimum load condition (after $t = 8$ s), some low-frequency pulsations are observed in the pressure signal. Additionally, Fig. 8c indicates that the variation of DT6 instantaneous mean in time is not significant. The extracted fluctuating signals (Fig. 8b and d) show maximum amplitudes of 2 kPa and 1 kPa in the vaneless space and draft tube, respectively. The level of pressure fluctuations of VL2 and DT6 sensors changes significantly over time. The low-frequency pulsations, due to flow structures in the draft tube, during part load and minimum load conditions, are also visible in both fluctuating pressure graphs.

Table 2
Validation of pressure and performance characteristics at BEP.

	Numerical	Experimental	Rel. Error (%)
VL2 pressure	173.98 kPa	173.54 kPa	0.25%
Shaft torque	629.68 N m	620.53 N m	1.47%
Net head	12.19 m	11.94 m	2.06%
Hydraulic Efficiency	91.84%	92.39%	0.60%

A Fast Fourier Transform (FFT) analysis was performed on the fluctuating signal at the BEP and minimum load parts of the sequence, as shown in Fig. 9. The VL2 results indicate a dominant frequency of $30f_n$ (f_n is the runner rotational frequency) at both BEP and minimum load, which corresponds to the runner blade passing frequency f_b (15 splitter blades and 15 full-length blades). The amplitude of this frequency is smaller at minimum load. Additionally, the harmonics of this dominant frequency, i.e., $15f_n$ and $60f_n$, are also excited. Several higher frequency harmonics are also captured (not shown here), due to the sufficiently small employed time step. The $15f_n$ can also be assumed as the full-length blade passing frequency (f_{mb}). The DT6 results show only a small excitement at the $f_{mb} = 15f_n$ frequency. This could be explained by the fact that only the 15 full-length blades are extended to the outlet of the runner. Moreover, a low-frequency band is amplified for both the VL2 and DT6 sensors at the minimum load condition which is related to the resolved large flow structures in the draft tube that produce high-amplitude low-frequency pulsations. The highest amplitude of this frequency band occurs approximately at $0.3f_n$.

Due to the variation in instantaneous mean values and dominant frequencies during the shutdown sequence, a Short Time Fourier Transform (STFT) analysis is required. In the STFT analysis, the whole time series is divided into many small time-spans for which a separate Fourier transform is performed. The results can be presented as a *spectrogram*, which reveals information about the variation of the amplitude of different frequencies in time. Fig. 10 provides spectrograms of the VL2 and DT6 pressure signals. The power of the pressure signal is shown in decibel (dB), computed as

$$P_{dB} = 10\log_{10}P. \tag{18}$$

It is seen in the VL2 results that the runner blade passing frequency ($f_b = 30f_n$) is dominant throughout the whole sequence and that its harmonics (e.g. $60f_n$) are also excited. A band of low-frequency pulsations caused by the formation of the RVR seems to start at $t = 4$ s and decay after $t = 6$ s due to the collapse and disintegration of the vortex rope. The amplitude of the low-frequency fluctuations grows in the minimum load condition. Also, a broad stochastic frequency span is observed at minimum load, which could be explained by the vortex shedding in the vaneless space. On the other hand, the spectrogram of the DT6 pressure signal shows a weaker sign of the blade passing frequency, whereas large flow structures in the draft tube such as the RVR seem to produce dominant low-frequency pressure fluctuations that start at $t = 4$ s and then decrease at $t = 6$ s. After the breakup of

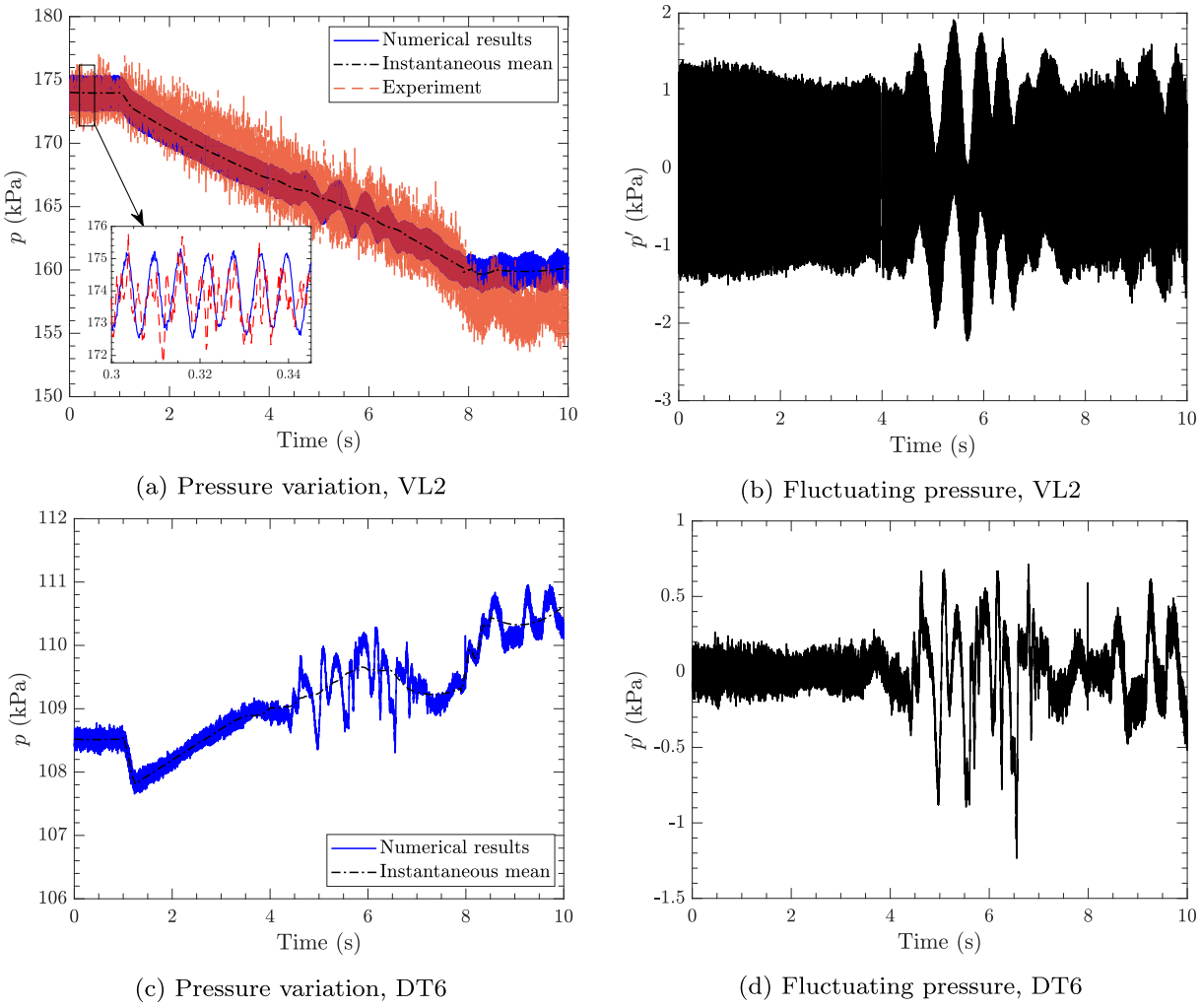

Fig. 8. Variation of static pressure in time for two probe locations during shutdown.

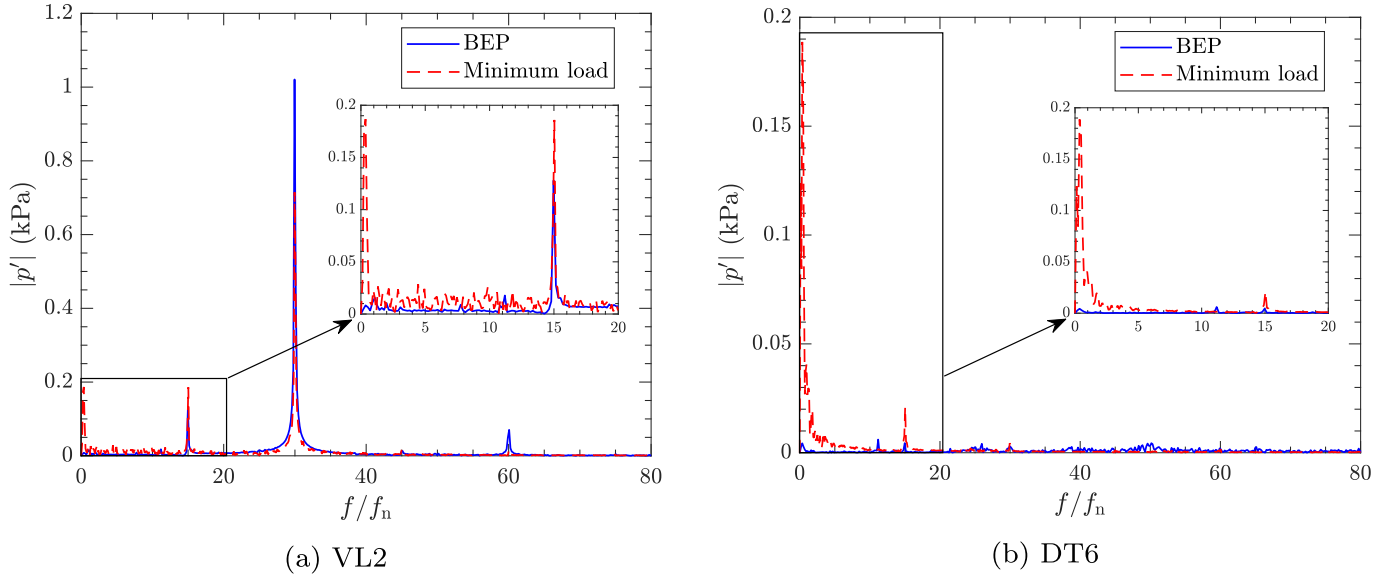

Fig. 9. Fast Fourier Transform of the fluctuating pressure in the stationary conditions at the beginning and end of the sequence (BEP and minimum load).

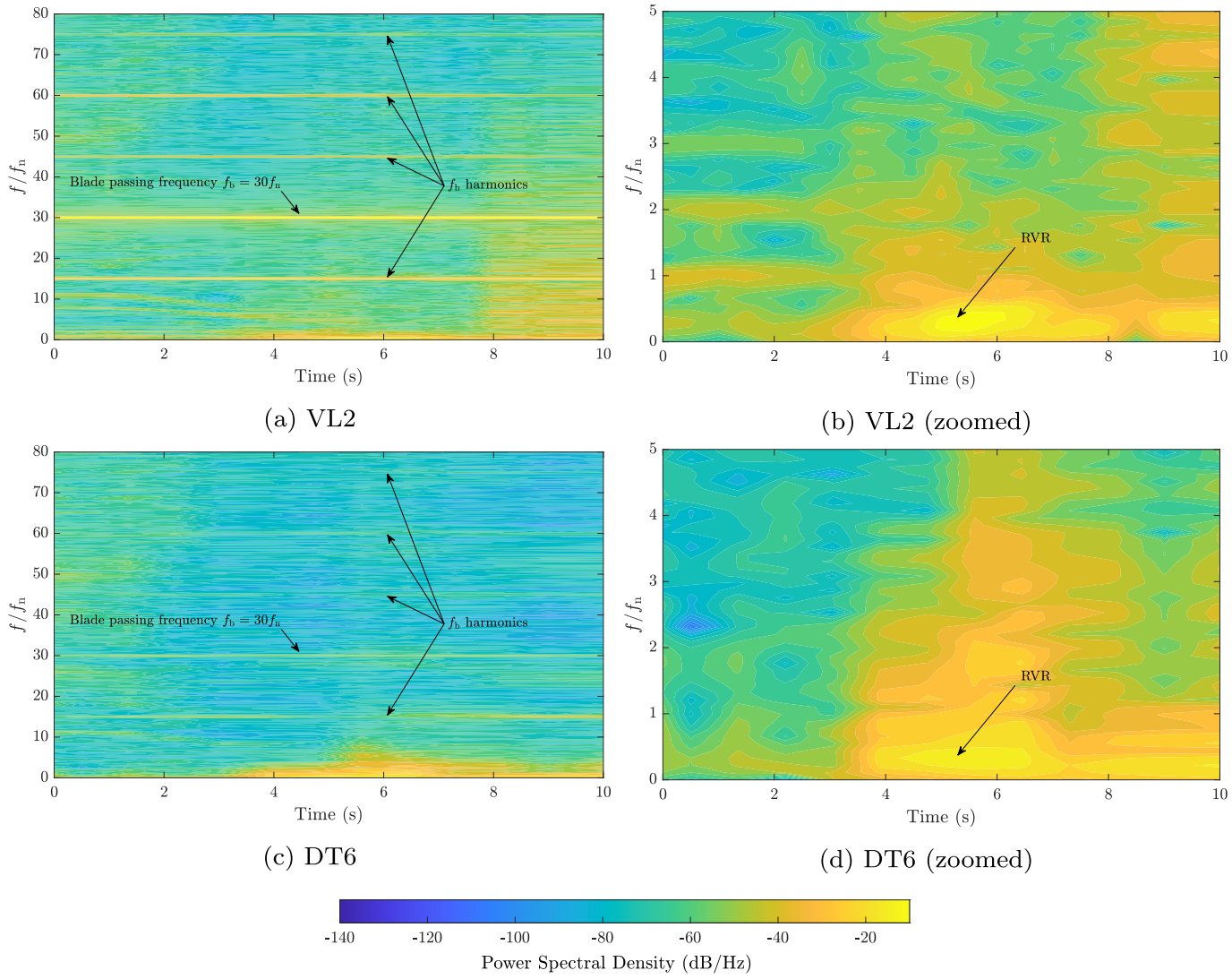

Fig. 10. Spectrogram of fluctuating pressure signal throughout shutdown sequence.

the vortex rope at $t = 6$ s, a wide range of stochastic frequencies appear (see particularly Fig. 10d). Later, the amplitudes of the low frequencies increase at the minimum load condition due to the recreation of large flow structures in the draft tube.

The time-dependent amplitudes of the main frequencies are extracted from the STFT analysis and shown in Fig. 11. The VL2 runner blade passing frequency ($30f_n$) is constant in the initial BEP condition ($t = 0$–1 s) and starts to reduce when the transient shutdown and flow rate reduction initiates. The amplitude slightly increases when the RVR breaks up (at $t = 6$ s), and then again decreases to a constant value in the minimum load condition. Most significant, the amplitude of the $0.3f_n$ frequency increases drastically after $t = 4$ s, indicating the formation of the RVR.

The wide range of frequencies observed in the frequency spectrum analysis can be classified into two categories, namely, deterministic and stochastic frequencies. The deterministic frequencies mostly originate from physical phenomena such as rotor-stator interaction, vortex rope, surge effects, etc., whereas the stochastic frequencies can arise from local flow structures, such as trailing edge vortex shedding, vortex break-down, as well as numerical errors (or measurement uncertainties in experiments). Generally, hydraulic turbines are expected to be dominated by deterministic frequencies at design conditions. The effect of stochastic frequencies becomes more significant at off-design conditions [5] where it may affect the lifetime of the machines [70,71]. A coherence analysis [72] may be performed to determine the deterministic and stochastic frequencies, revealing information about the correlation (level of in-phase or out-of-phase) between the pressure signals in the different probes.

The time-dependent coherences between the fluctuating pressure signals of the VL2, DT5, and DT6 probes are shown in Fig. 12. The coherence between the signals of the VL2 sensor (in the vaneless space) and DT6 (in the draft tube) can reveal the global deterministic frequencies. The coherence between the signals of the DT5 and DT6 sensors (both in draft tube and 180° apart) specifies the draft tube local frequencies. It is seen in Fig. 12a that the runner blade frequency ($30f_n$) and half that frequency ($15f_n$, corresponding to the full-length runner blades) are always in-phase between the VL2 and DT6 sensors, with a coherence of one. However, other frequencies, that are mostly related to local flow conditions, are out-of-phase and thus give a small coherence. On the other hand, the coherence between DT5 and DT6 (in Fig. 12b) shows that all the frequencies at BEP are in-phase. As expected, an attached flow field should exist in the draft tube at BEP with no significant local vortical structures, meaning that although DT5 and DT6 are located at opposite sides of the draft tube cone,

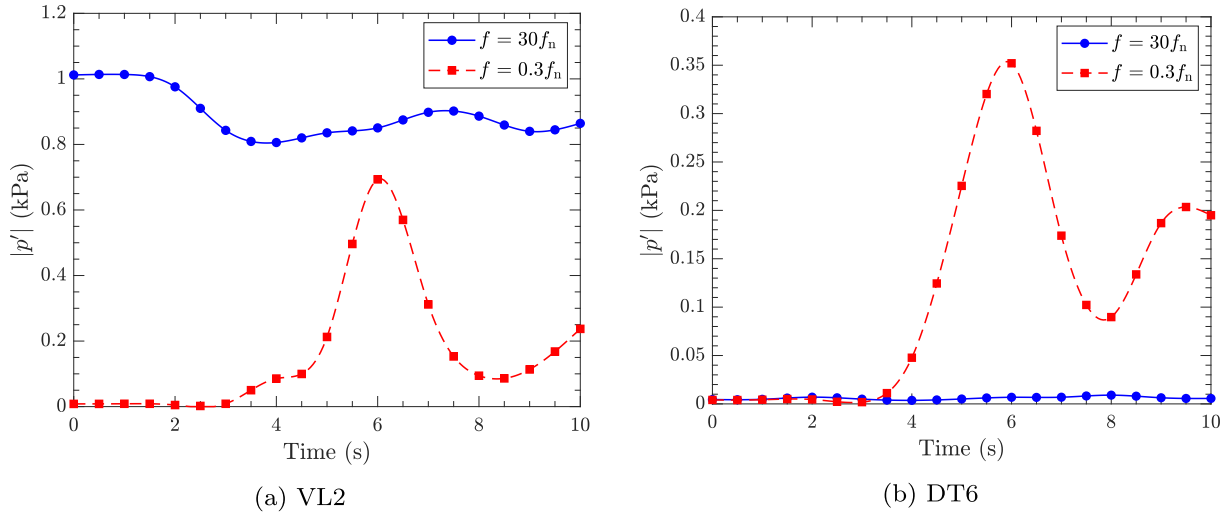

Fig. 11. Variation of fluctuating pressure amplitude over time.

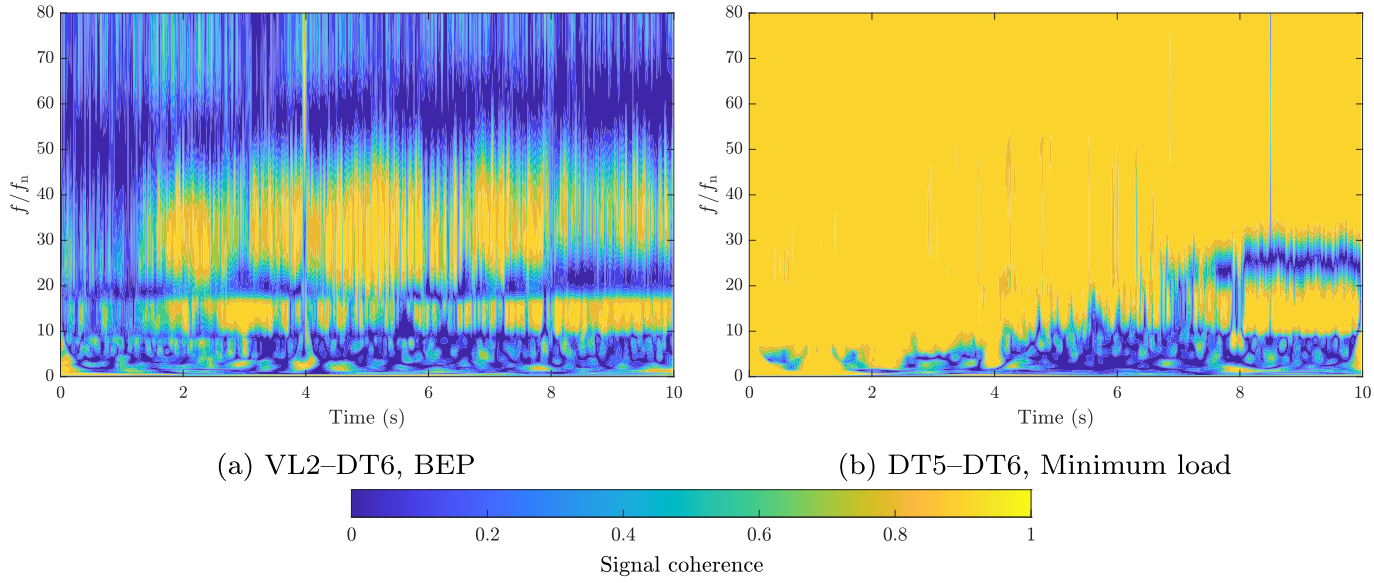

Fig. 12. Time-dependent coherence of fluctuating pressure signals of VL2, DT5, and DT6 probes in the full shutdown sequence.

they experience nearly the same flow conditions. Nevertheless, when the transient shutdown sequence initiates, a stagnant region develops which results in the formation and collapse of local vortices with different time and length scales. Consequently, stochastic low-frequency fluctuations are generated and expanded to a wide range of frequencies as the shutdown sequence proceeds, which can be detected as an out-of-phase region with small signal coherence in Fig. 12b. This wide range of frequencies is cut by the coherent full-length runner blade passing frequency ($15f_n$), as can be most clearly seen at the end of the time series. This frequency is related to the trailing edges of the full-length runner blades, and their wakes that are advected into the draft tube.

The four additional pressure probe locations GV1, GV2, GV3, and GV4, shown in Fig. 13, are here used for a thorough analysis of the flow behavior in that region. The variation of static pressure and the amplitude of its fluctuations from the instantaneous mean value are found in Fig. 14. The GV1 and GV2 pressures increase during the shutdown sequence, while the GV3 and GV4 pressures decrease. This could be explained through the positioning of these probes with respect to the touching location of guide vanes in a fully closed situation. As seen in Fig. 13, when the guide vanes are fully closed the GV1 and GV2 probes will be located on the upstream side of the guide vanes (casing side) while GV3 and GV4 are on the downstream (runner side). Thus, GV1 and GV2 pressures increases because of flow rate reduction, and whilst GV3 and GV4 pressure reduce due to augmentation of guide vanes pressure drop through the reducing clearance between the guide vanes. Ultimately, at a full shutdown procedure, when the guide vanes are fully closed and flow rate is zero, the GV1 and GV2 pressures approach turbine inlet pressure whereas GV3 and GV4 pressures reach turbine outlet pressure. A zoomed view of the pressure fluctuations at BEP during 90° of runner rotation is shown in Fig. 14b. The effect of RSI fluctuations is clearly visible in all probes and their magnitudes decrease with distance from the runner blades. However, at the minimum load condition (Fig. 14c) it is the GV3 probe that shows the strongest fluctuations, with an additional frequency of roughly half the runner blade passing frequency.

Fig. 15 shows the time-variation of amplitudes of the blade

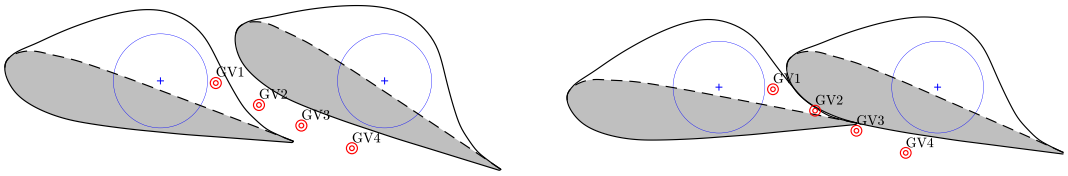

(a) BEP, $\alpha = 9.84°$ (b) Fully closed, $\alpha = 0°$

Fig. 13. Locations of guide vane domain numerical pressure probes.

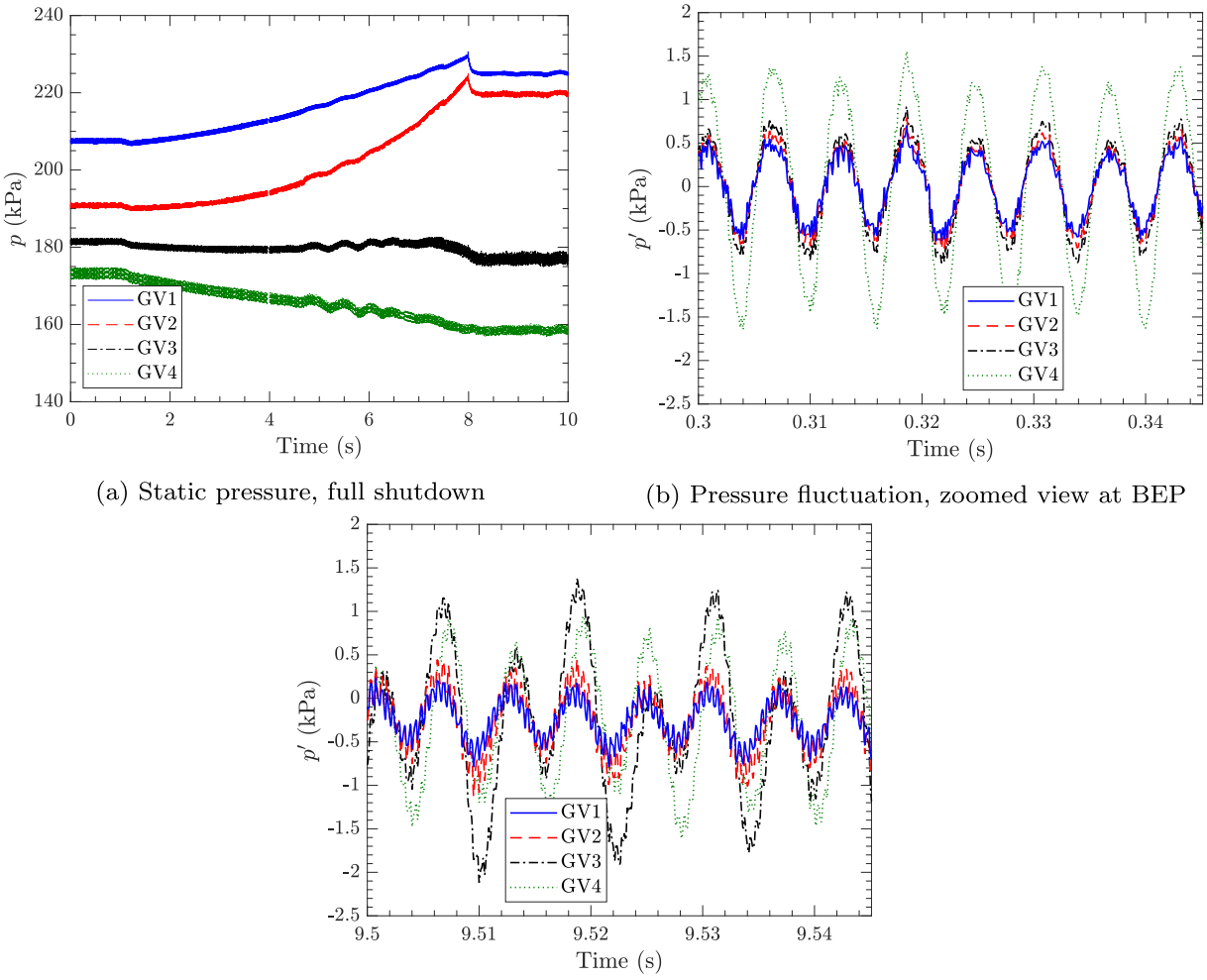

(a) Static pressure, full shutdown

(b) Pressure fluctuation, zoomed view at BEP

(c) Pressure fluctuation, zoomed view at minimum load

Fig. 14. Static pressure variation at the guide vane domain numerical pressure probes.

passing frequencies ($15f_n$ and $30f_n$) at the four probes during the transient sequence. The GV3 amplitude increases substantially for both frequencies after $t = 6$ s, while the amplitudes for the other probes are nearly constant for $15f_n$ and decrease for $30f_n$. The increase in the GV3 amplitudes happens to be at the same time as when the vortex rope starts to break up, but if the vortex rope breakup would be the cause it should affect the GV4 probe the same way. A more likely reason is that a guide vane trailing edge separation frequency (e.g. vortex shedding) is captured by the GV3 probe, possibly amplified due to interaction with the runner blade passing frequency. The vortical structures presented using isosurfaces of $\lambda_2 = 7500$ s^{-2} (more information on the λ_2 vortex identification method is given in Section 4.2.4) in Fig. 16 indicate a complex flow field near the guide vane trailing edges at minimum load condition, which could explain the rise in amplitude of the GV3 $15f_n$ frequency.

Fig. 17 presents the coherence between the GV1 and GV4 pressure fluctuations. A strong coherence is visible at BEP, where almost all frequencies are in phase. However, when the turbine moves to the part load condition, stochastic low frequencies associated with different flow structures (such as trailing edge separation and vortex rope breakup) become more and more out-of-phase. Despite that, the deterministic frequencies (blade passing frequency and its harmonics) remain in phase, even in the minimum load condition.

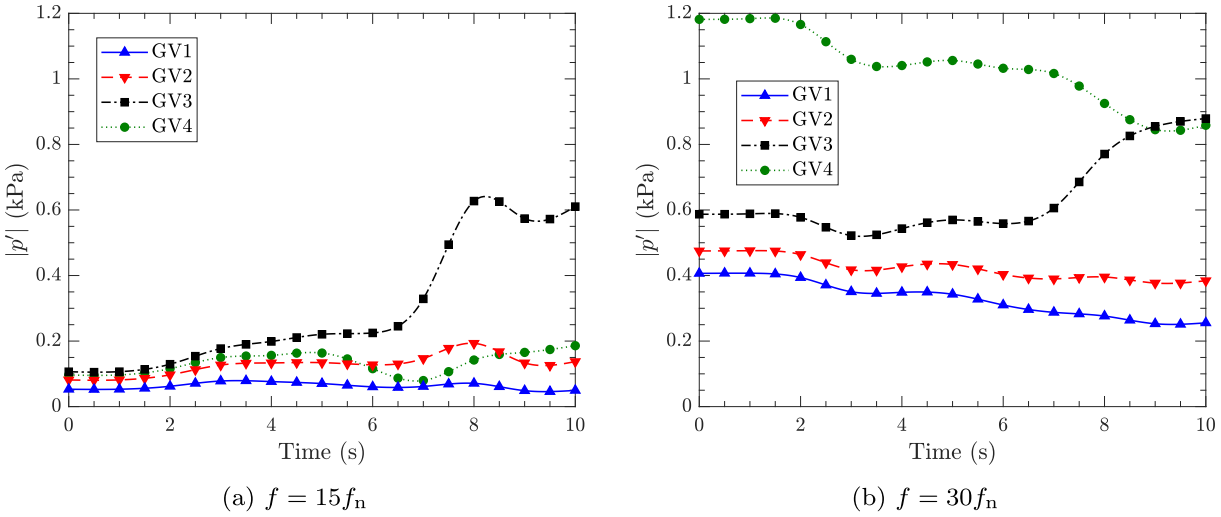

Fig. 15. Variation of fluctuations amplitude at the guide vane domain numerical pressure probes.

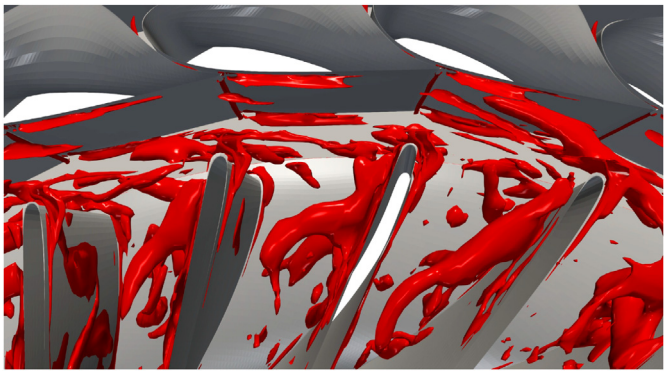

Fig. 16. Iso-surface of $\lambda_2 = 7500\ s^{-2}$, displaying vortex shedding near guide vane trailing edges at minimum load condition.

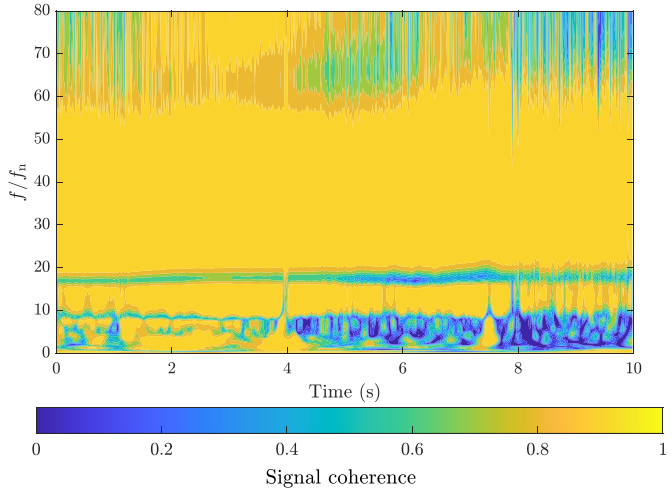

Fig. 17. Time-dependent coherence of fluctuating pressure signals of GV1 and GV4.

4.2.2. Force analysis

It is of utmost importance to conduct a force analysis of hydraulic turbines during transient operation since fluctuating forces could seriously affect the lifetime of the machines. An investigation of the forces exerted on the runner surfaces (i.e., hub, band, full-length blades, and splitter blades) is here conducted.

The x (horizontal) and z (axial) components of the force exerted on the runner are plotted in Fig. 18. The y-direction force is similar to that of the x-direction and is omitted here for brevity. As expected, the forces are mostly originating from the static pressure and the viscous forces are comparatively small. It is seen that F_x oscillates around a non-zero positive value at the BEP condition. It means that the incoming flow to the runner is not distributed fully axisymmetric, which is not ideal. Large oscillations appear in F_x after $t = 4$ s when the vortex rope is formed, and the oscillations are dampened as the vortex collapses. A weaker low-frequency oscillation is established at the minimum load condition. The axial force, F_z, decreases with the load reduction. It is initially positive (upward) due to the pressure distribution of the runner. At around $t = 4$ s, when the vortex rope is formed, F_z becomes negative owing to the creation of a large low-pressure separated flow region in the draft tube near the runner outlet. The fluctuating part of the axial force (F_z') also shows large oscillations both between $t = 4$ s and $t = 7$ s and at minimum load condition. The oscillations of axial force at the minimum load are much larger than the corresponding oscillations of the horizontal force. This shows that the large instabilities at minimum load are mostly of plunging type.

An STFT analysis is performed on the runner forces and the results are exhibited as spectrograms in Fig. 19. The runner blade frequency, denoted by f_b, is a deterministic dominant frequency throughout the entire shutdown sequence. Furthermore, its harmonics are also excited and visible in the spectrogram contours. It can be seen in the zoomed view of F_x (Fig. 19b) that also the runner rotation frequency (f_n) is significant until $t = 4$ s. This frequency was also seen at the BEP condition in Fig. 18a, where the force has a low-frequency oscillating mode with a period of approximately 0.18 s, corresponding to the runner rotation. It diminishes as the RVR is formed, and vanishes in a broad range of stochastic frequencies at the minimum load condition. Another high-deterministic frequency is seen around $11.2f_b$ at the BEP condition, for both the horizontal and axial forces. The frequency and its amplitude are both reduced during the initial part of the shutdown sequence, and it vanishes before $t = 4$ s. The reduction of the excited frequency during the transient sequence suggests that the frequency is not induced by the rotor-stator interaction, since the rotational speed remains constant. Instead, it should be correlated to a flow structure that exists at the BEP condition and then decays during the

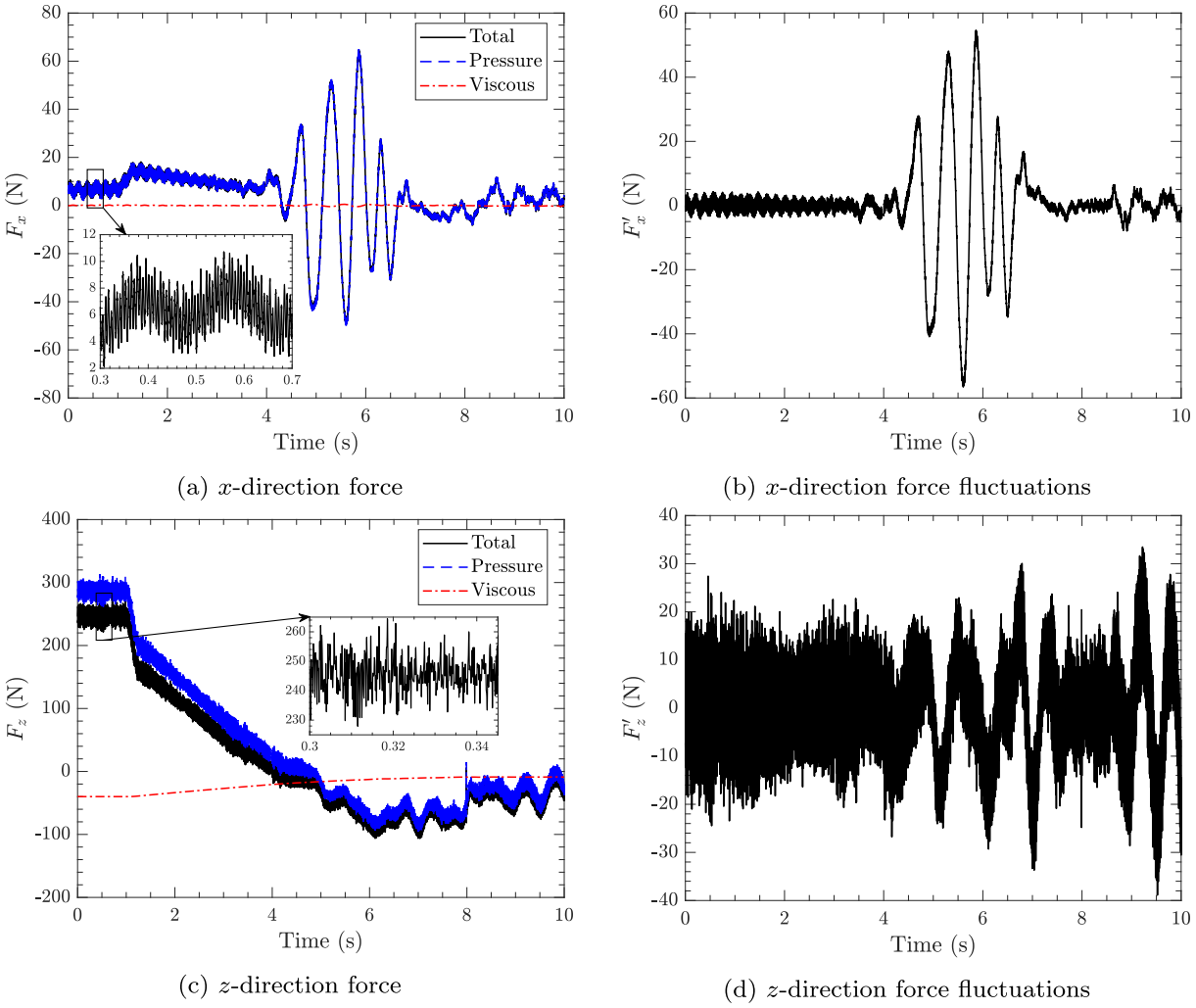

Fig. 18. Variation of components of forces exerted on the runner during shutdown sequence.

shutdown sequence. The frequency might be related to a resolved oscillating von Kármán street behind the guide vanes trailing edges, runner blades trailing edges, or blunt runner cone. Vibrations due to von Kármán vortex streets occur frequently in hydraulic turbines [73]. However, the definite origin of this frequency is not yet clear and requires further investigations.

The axial force spectrogram has less distinct frequencies, indicating a wide range of stochastic fluctuations throughout the whole shutdown sequence. In other words, stochastic frequencies originating from small local flow structures mostly influence the axial force rather than the horizontal force. This is also noticeable in the zoomed views of Fig. 18a and c, where the F_z fluctuations are more chaotic than the F_x fluctuations. Further, the amplitude of $11.2f_b$ frequency is smaller for the axial force than for the horizontal force.

4.2.3. Velocity field variation

The experimentally measured velocity field is available for the entire shutdown sequence along the three lines shown in Fig. 2. The present numerical results are compared with the experimental data to validate the results and to give a better understanding of the draft tube flow field during the turbine shutdown.

The time-variation of the numerical and experimental results of the axial (W), horizontal (U), and normal (V) velocity components along the three PIV lines are shown in Figs. 20–22. The comparison of the axial velocity component reveals a very good similarity between the numerical and experimental results at all three lines. Lines 1 and 2 show rather similar trends through time in both sets of results. The contours display a statistically quasi-steady flow field at BEP ($t < 1$ s). The magnitude of the axial velocity first increases when going from the draft tube walls ($s/s_{max} = 0, 1$) to the center ($s/s_{max} = 0.5$), and then slightly decreases at the center because of the wake behind the runner cone. This was also seen in the time-averaged axial velocity profiles at BEP in Fig. 7. The numerical results at BEP reveal small temporal oscillations at the center, most likely due to the von Kármán vortex street behind the runner blunt cone. When the transient sequence starts to reduce the flow rate at $t = 1$ s the magnitude of the axial velocity initially decreases mostly in the region $0.1 < s/s_{max} < 0.9$. At $t = 4$ s, when the RVR starts forming, the reduction of the magnitude of the axial velocity reaches further out. The inception of a reversed flow region is observed at the center of both Lines 1 and 2, at about $t = 2.25$ s and $t = 2.6$ s for the numerical and experimental results, respectively. The recirculation region expands with a conical shape in time and forces the main flow to the periphery of the draft tube. After $t = 6$ s the reversed flow region covers the entire PIV lines, and a massively separated flow field occurs downstream the runner at the minimum load condition. Large oscillations in the axial velocity are visible due to the RVR between $t = 4$ s and $t = 6$ s, which decreases after the disintegration of vortex rope. The axial velocity on Line 3 shows the same inception of the recirculation as discussed for Lines

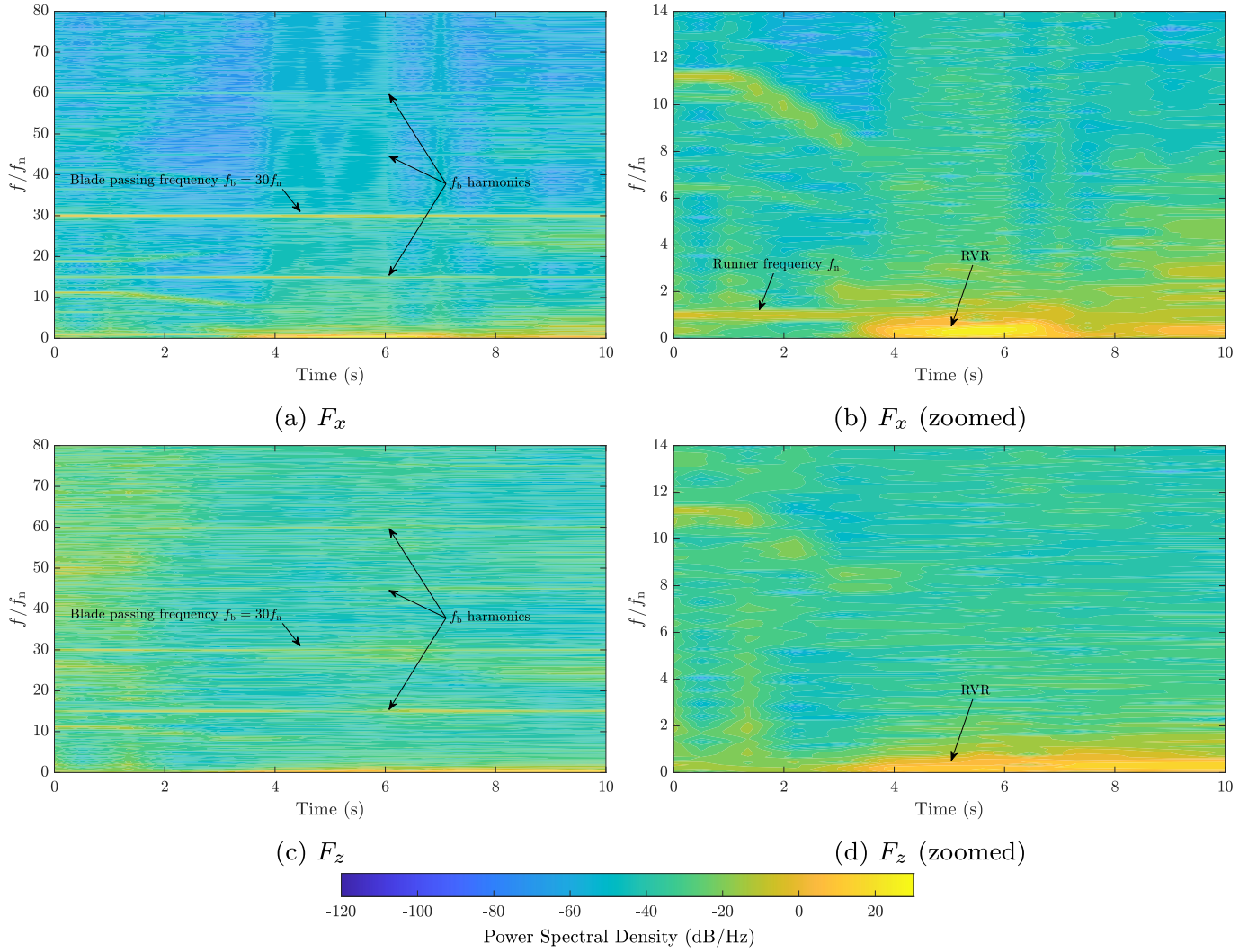

Fig. 19. Spectrogram of fluctuating forces.

1 and 2, at $t = 2.25$ s and $t = 2.6$ s for the numerical and experimental results, respectively. It can be seen that the inception occurs instantly along the entire Line 3, as a sudden change in flow characteristics in the draft tube [74].

The horizontal velocity component (Fig. 21) is mostly oscillating around zero. It is most obvious in the numerical results that the horizontal velocity oscillations are temporarily increased between $t = 4$ s and $t = 6$ s when the RVR is formed in the draft tube. As the RVR collapses, the large oscillations dampen out and again go back to smaller fluctuations around zero. A similar effect can also be seen in the experimental data, although with smaller amplitudes. It is first of all important to remember that the time-averaged results at BEP showed that the experimental data was not taken at the center of the vortex, as discussed in Section 4.1. This could also have some effect on this transient analysis. One must also realize that the sampling frequency of the instantaneous PIV measurements is rather low and that such data is often averaged over both a small time window and over a small spatial region. Such averaging smoothens out fluctuations. Given that the numerical and experimental data show similar behavior, the numerical results are validated and extend the experimental results with additional resolution of the unsteady effects.

The time-variation of the numerical normal velocity component is also illustrated in Fig. 22. It should be recalled that no experimental data is available for this component. A weak swirling flow seems to exist on Lines 1 and 2 at the BEP condition. When the shutdown initiates, the swirl direction changes and the normal velocity magnitude gradually enhances as the flow rate reduces. The physical explanation for the change in the swirl direction and magnitude is presented later in the current section. In the part load condition, the formation of the RVR makes the swirling flow unstable and the vortex center (zero normal velocity) oscillate remarkably between $t = 4$ s and $t = 6$ s. After that, the central stagnant region, corresponding to near-zero normal velocities, expands and the RVR collapses. The same effect is seen on Line 3, where the magnitude of the normal velocity is always near zero, except for the period in which the RVR is formed.

Since a URANS simulation is performed, it is expected that some portion of turbulent kinetic energy is resolved. The ratio between resolved and total turbulent kinetic energy defined as

$$r = \frac{k_{\text{resolved}}}{k_{\text{resolved}} + k_{\text{modeled}}}, \tag{19}$$

helps to identify how well resolved the captured structures are. k_{resolved} can be computed through

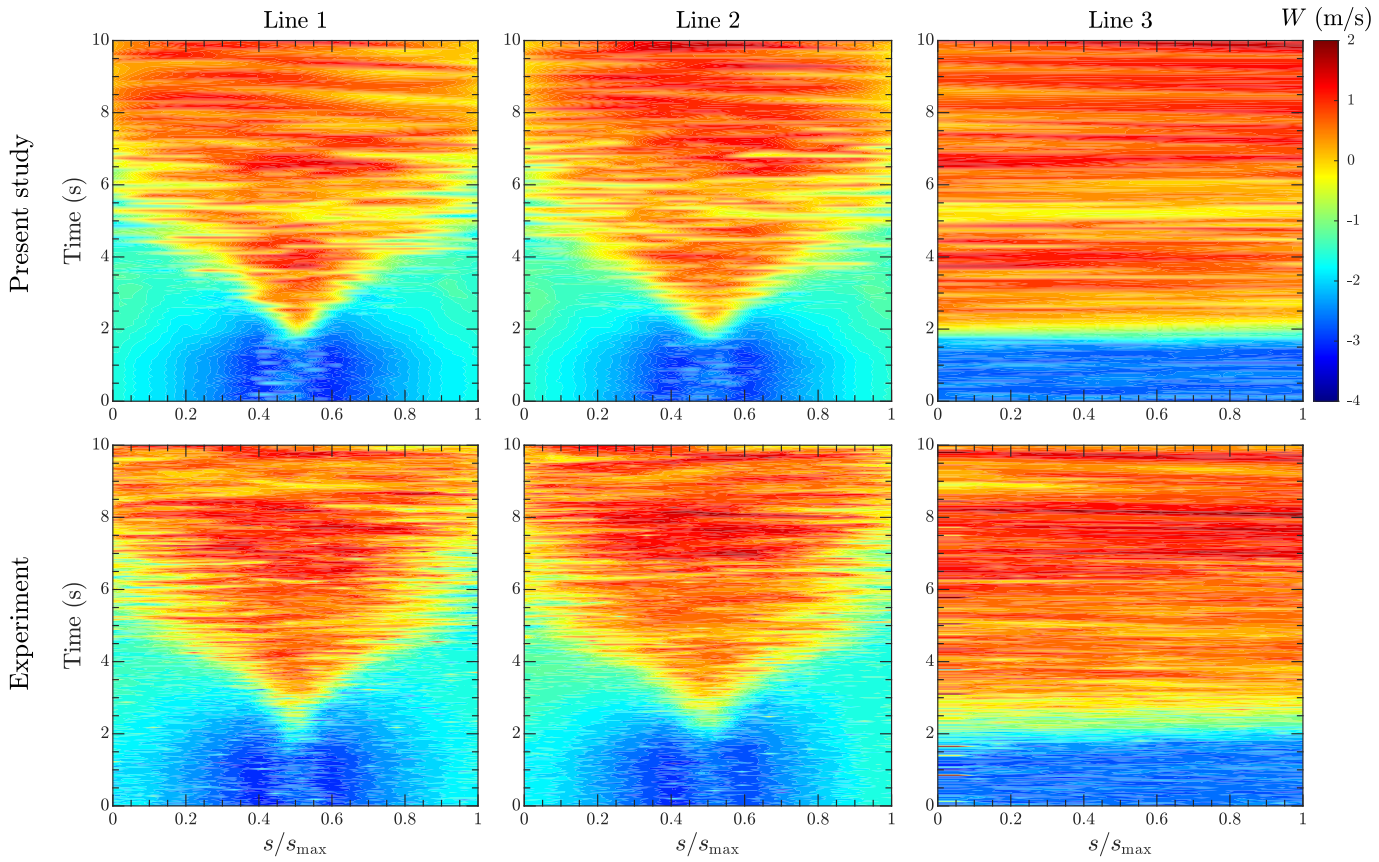

Fig. 20. Time-variation of axial velocity (W) along experimental PIV lines.

$$k_{\text{resolved}} = \frac{1}{2}\sum_{i=1}^{3}\overline{u}_i^{\,2}, \tag{20}$$

where u_i is the fluctuating part of velocity in direction i, calculated using window averaging. Fig. 23 displays the time-variation of the above-explained ratio r during shutdown sequence. At BEP the ratio is near one in around the center, indicating well resolution of the central flow structures of the draft tube. When the shutdown starts, the ratio increases, and between $t = 4$ s and $t = 6$ s is near one on the whole Line 1 and 2. In other words, the draft tube structures, such as RVR, are well resolved in the current study.

In order to perform further analysis of the velocity field, Points 1 and 2 are defined on Line 1 (see Fig. 2) and the velocity components are compared in Fig. 24. The radius of the points are $R_{\text{Point1}} = 46.5$ mm and $R_{\text{Point2}} = 106.2$ mm, corresponding the normalized curve lengths of $s/s_{\text{max}} = 0.332$ and 0.075, respectively. Thus, Point 1 is close to the axis while Point 2 is nearer to the wall. As explained for the velocity contours in Figs. 20–22, the horizontal velocity fluctuates around a near-zero instantaneous mean. The horizontal velocity fluctuations grow significantly after $t = 2.5$ s in Point 1, while a corresponding growth in Point 2 starts later at $t = 3.5$ s. This shows that a vortical structure is initiated close to the center since it affects Point 1 sooner than Point 2. The structure grows radially in time, and eventually reaches Point 2. This was also seen in Fig. 21, where a weak conical shape is developing in the middle. Large oscillations are visible after the creation of the RVR. They decay as the RVR diminishes and reach a moderate level at minimum load. Both instantaneous mean and fluctuation amplitudes are in acceptable agreement with the experimental data. However, it can be seen that the numerical results reveal a slightly more deterministic signal during the time of the vortex rope. This difference can be due to limited resolution in the PIV sampling frequency, or due to the modeling of the smallest scales in the numerical results.

The magnitude of the axial velocity reduces in both points when the guide vanes start to close down (which is directly related to a reduction in flow rate through the machine). The reduction rate is sharper for Point 1 because it is close to the center and is more affected by the formation of the vortex rope. The recirculation region, determined by $W \geq 0$, reaches Point 1 at about $t = 4$s and Point 2 at about $t = 6s$. The numerical and experimental data show similar values for both trends and fluctuations of the axial velocity component. It is worth mentioning that the y-axis range of the W plot is larger and thus the velocity fluctuations may seem smaller.

The normal velocity component, V, is also presented in Fig. 24 to assess the swirling flow in the draft tube. No experimental data is available to compare with, due to limitations in the experimental setup. On these points, a positive V is in the same direction of the runner rotation, according to the right-hand rule and the definition of the axial direction. In order to understand the variation of the swirling flow during the load variation one can look at the velocity triangles at the runner blade trailing edge, shown in Fig. 25. Notations $\vec{\mathcal{U}}$, $\vec{\mathcal{W}}$, and $\vec{\mathcal{C}}$ represent the blade rotating (circumferential) velocity vector, the fluid relative velocity vector, and the fluid absolute velocity vector, respectively. The rotational speed of the runner is constant during the transient sequence. Therefore, the magnitude and direction of the $\vec{\mathcal{U}}$ vector are fixed at all conditions. The β_2 angle measures the angle between the relative velocity vector and the blade velocity vector at the runner trailing edge.

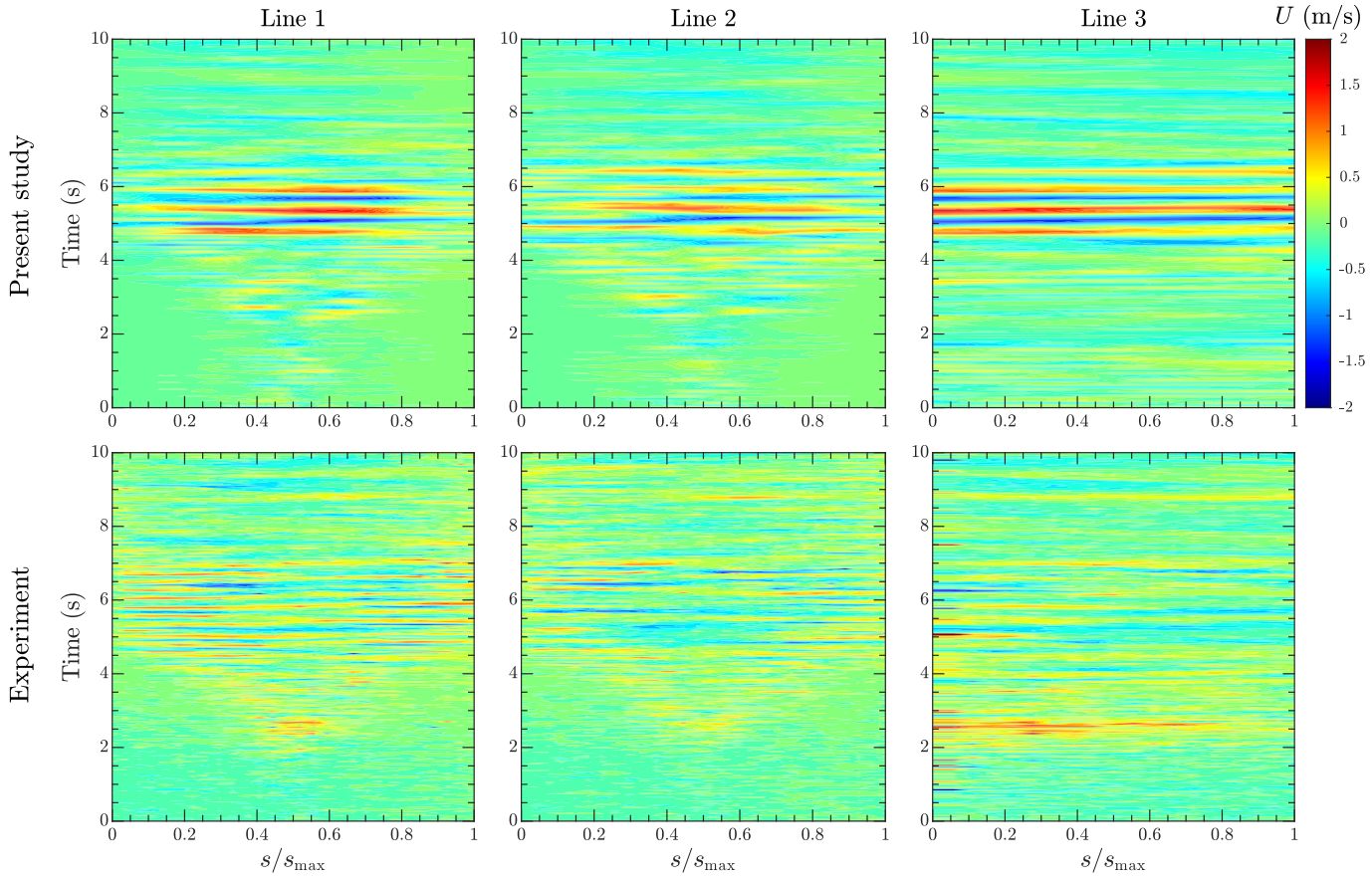

Fig. 21. Time-variation of horizontal velocity (U) along experimental PIV lines.

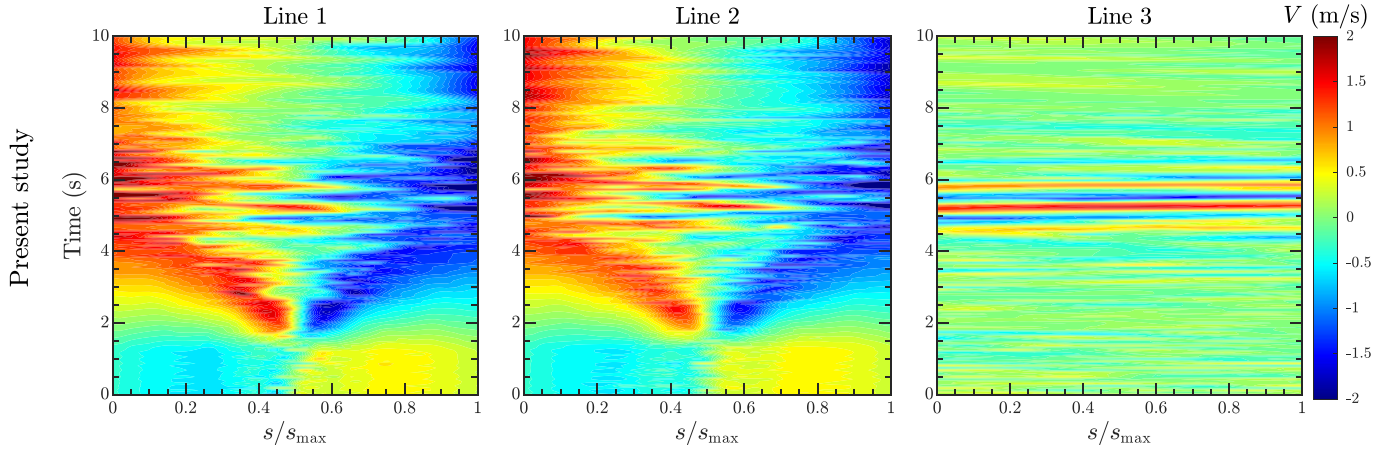

Fig. 22. Time-variation of normal velocity (V) along experimental PIV lines.

Assuming that the flow is ideally guided by the blade at the trailing edge, β_2 is constant during the entire shutdown sequence. The meridional velocity vector (C_m) is linearly correlated to the flow rate. Water turbines are designed to have a circumferential component (C_u) close to zero after the runner, at BEP, for which the flow leaves the runner without any swirl (Fig. 25b). A higher flow rate (high load) creates a negative (counter-rotating) swirl (Fig. 25a), whereas a lower flow rate created a positive residual swirl in the draft tube (Fig. 25c). Although the velocity triangle theory might not be accurately valid throughout the whole shutdown sequence, it still helps to understand the variation of swirling flow exiting the runner.

The tangential velocity component in Points 1 and 2 has a small negative value during the BEP condition, meaning that the draft tube flow has a low-intensity swirl in the opposite direction of the runner rotation. In other words, the velocity triangle is slightly shifted towards high load (Fig. 25a) at the beginning. A weak swirling flow in the draft tube might be intentional in the design as it can help the flow to stay attached to the draft tube walls and therefore maintain the high efficiency of the machine. As the flow

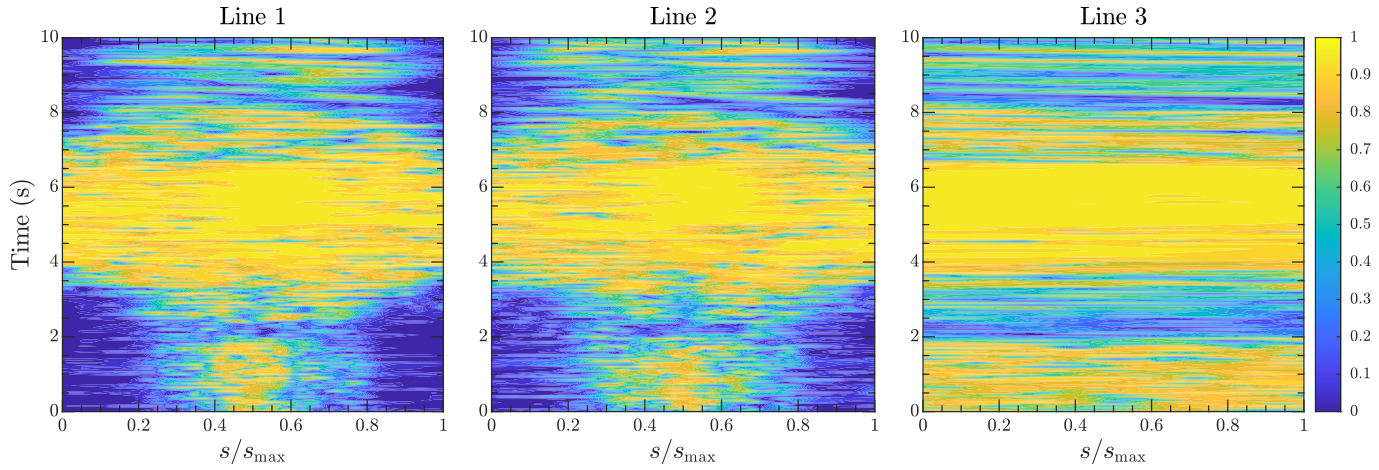

Fig. 23. Time-variation of the ratio of resolved and total turbulent kinetic energy along experimental PIV lines.

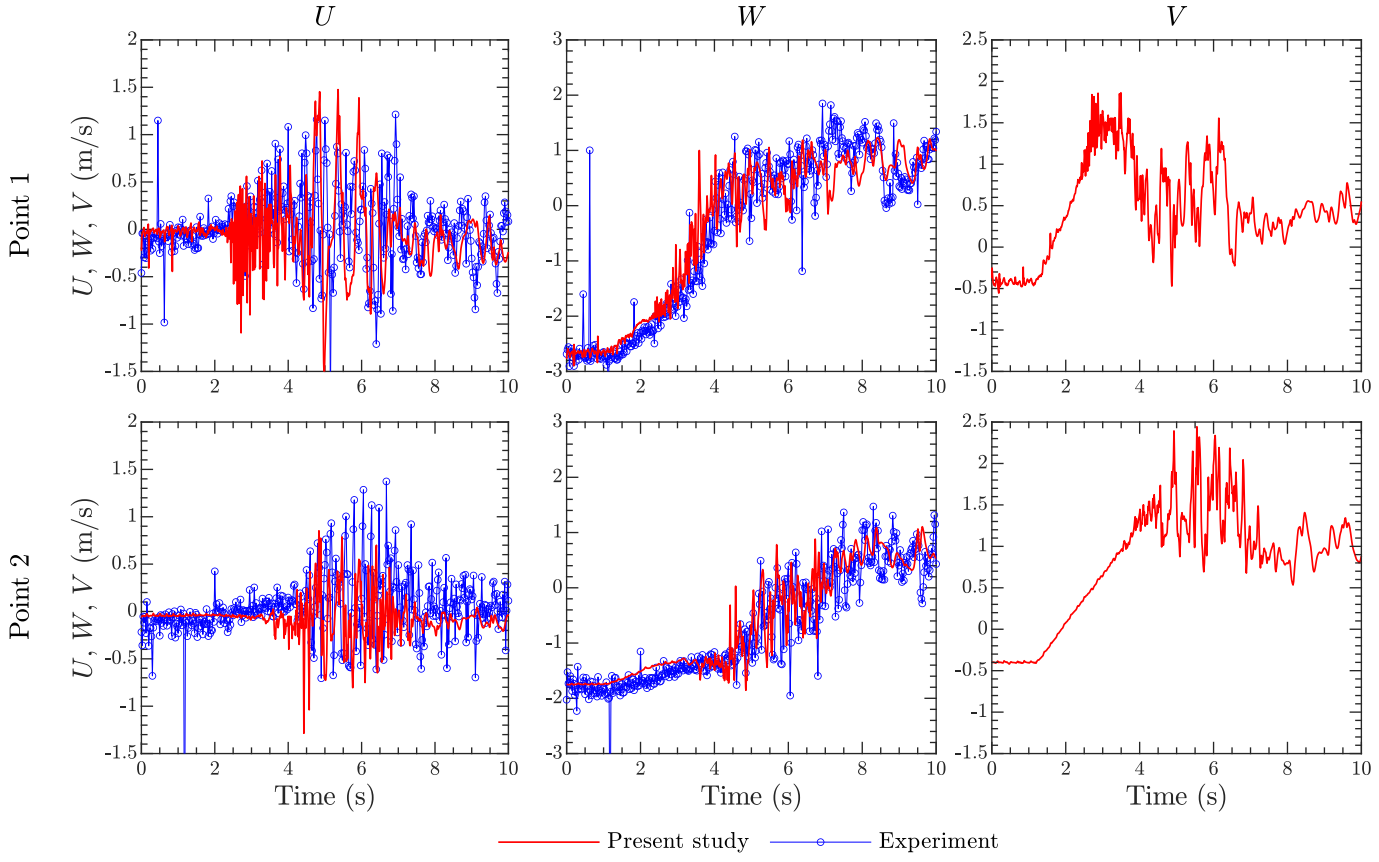

Fig. 24. Time-variation of horizontal (U), axial (W), and normal (V) velocity components on Points 1 and 2 compared to the experimental PIV data.

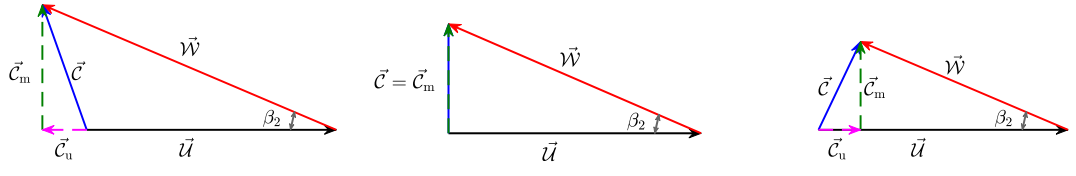

Fig. 25. Velocity triangles on the runner trailing edge at different operating conditions.

rate decreases, the absolute tangential velocity component becomes zero and the flow is thus locally momentarily non-swirling. However, it can be seen that the tangential absolute velocity becomes zero at slightly different times in Points 1 and 2, suggesting a more complex flow than the ideal one that can be described with velocity triangles. A further reduction of the flow rate creates and intensifies a swirl in the runner rotational direction. After a while, the development of the RVR and its collapse results in fluctuating tangential velocities. Point 1, which is closer to the inception of the RVR, experiences the RVR sooner.

4.2.4. Flow structures in the draft tube

This section is dedicated to investigating the flow structures that are formed in the draft tube during the shutdown sequence. Different methods are proposed and utilized in the literature to find and display vortices in hydroturbines, For example, iso-surface of static pressure, Q-criterion, Δ-criterion, λ_2-criterion, streamlines, vorticity, helicity, etc [75]. Both the Q and λ_2-criterion methods have been evaluated in the present analysis, and it was concluded that they reveal rather similar flow structures in the draft tube of the current case study. Therefore, the λ_2 vortex identification method [76] is utilized in this study to identify and visualize the draft tube vortical structures, such as the rotating vortex rope. It can be shown that a vortex is a region with two negative eigenvalues of the $\boldsymbol{S}^2 + \boldsymbol{\Omega}^2$ tensor, where $\boldsymbol{S}$ and $\boldsymbol{\Omega}$ are the strain and rotation tensors

$$\boldsymbol{S} = \frac{1}{2}\left(\nabla U + \nabla U^{\mathrm{T}}\right), \quad \boldsymbol{\Omega} = \frac{1}{2}\left(\nabla U - \nabla U^{\mathrm{T}}\right) \tag{21}$$

Therefore, the second largest eigenvalue, λ_2, is negative inside a vortex, and the vortex can be identified by an iso-surface of a negative value of λ_2. It should be mentioned that in OpenFOAM the eigenvalues of the $\boldsymbol{S}^2 + \boldsymbol{\Omega}^2$ tensor are given a negative sign after they are computed, and therefore a positive value should be used for the iso-surfaces. The λ_2 method has been successfully employed to identify rotating vortex rope structures in Francis turbine draft tube [14].

Fig. 26 presents vortical structures in the draft tube at different times during the turbine shutdown sequence. The value for λ_2 iso-surfaces was tuned to get the best visualization of vortical structures in the draft tube and $\lambda_2 = 750\ \mathrm{s}^{-2}$ is employed for this purpose. Additionally, in each figure, in-plane velocity vectors are shown in three sections, demonstrating the secondary flow field. Besides the time, the guide vane opening angle (α), and the turbine load (normalized flow rate Q/Q_{BEP}) are presented for clarity.

The iso-surface shows a narrow vortex rope at BEP ($t = 0$–1 s, Fig. 26a). The vortex is nearly stationary at the design condition. The velocity vectors show a weak counter-rotating vortex due to a negative swirl residual at the outlet of the runner. The swirl seems to enhance downstream, which is most likely due to the effect of secondary flows of the downstream elbow. When the transient sequence starts, at $t = 1$ s, the flow rate decreases, and thus the negative swirl residual reduces and becomes momentarily zero (see Fig. 25). Therefore, the slender vortex rope vanishes around $t = 1.6$ s (Fig. 26b). The secondary flow vectors also indicate that the flow is almost swirl-free at the first section, while a negative swirl is still visible at the second and third sections, showing that the change in the runner outlet velocity triangle has not reached so far yet.

Thereafter, with further closing of the guide vanes, the turbine goes into the part load condition (Fig. 26c), where the runner does not completely extract the angular momentum of the flow and a positive residual swirl remains at the outlet of the runner (Fig. 25c). As previously shown in Fig. 20, after $t = 2$ s the central high axial velocity magnitude region diminishes, and a stagnant region develops at the axis. Consequently, a stationary vortex rope establishes at the center of the draft tube and develops both radially and axially through time, due to the enhancement of swirling flow. The in-plane vectors at the first and second cross-sections support this analysis, where a positive swirl is visible which is stronger around the center. On the contrary, the secondary flow at the third cross-section has not yet sensed the change in the swirl direction and is still counter-rotating.

Later on, at $t = 3$ s (Fig. 26d), the central stagnant region develops and the vortex rope core expands. Then the core becomes unstable and complex rotating vortical structures are created from the runner hub. Subsequently, with additional load reduction at $t = 3.6$ s (Fig. 26e), the instability of the central vortex splits the core into different vortices that rotate around the central axis. The downstream part of the initial vortex core is detached and washed away. At this time two long vortex ropes are visible that are attached to the runner cone. Furthermore, a few smaller vortical structures are also generated. Moreover, the positive swirl, shown by the tangential vectors at the three sections, is getting stronger as the turbine goes more deeply into the part load condition.

Fig. 26f demonstrates the draft tube flow structures at the time $t = 4.2$ s, which has in the previous sections been identified as the start time for the formation of the rotating vortex rope and its accompanying high-amplitude fluctuations. Although not a single RVR structure is visible at $t = 4.2$ s, the helical vortex structures are developing and getting more unstable. Then, after some time, some of these vortical structures are merged together and create one large rotating structure, as seen in Fig. 26g at $t = 4.8$ s. Many small vortical structures that are not integrated into the RVR are detached and washed away with the flow. The velocity vectors still show an enhancement of positive swirl due to the load reduction that results in an increasing residual of angular momentum. The physical process of the formation and collapse of the RVR is further discussed later in this section.

The RVR rotates around the draft tube axis due to the instability of the shear layer at the interface of the swirling outer and central stagnant regions and stands in a new position at time $t = 5.4$ s (Fig. 26h). In contrast to a stationary part load condition, where a stable RVR stays in the draft tube, the RVR does not remain stable during the continuation of the shutdown sequence. The number of detached small vortical structures increases in time. A while later, at time $t = 6$ s (Fig. 26i), the RVR is fully disintegrated into smaller vortical structures that are not coherent and are washed away after creation. At this point in time the RVR breaks up and the high-amplitude pulsations end.

Hereafter, only small vortices are formed and carried away with the upstream flow, which causes a broad range of stochastic frequencies (Fig. 26j). This can be seen in Fig. 10d, where after the vanishing RVR a wide range of frequencies are visible in the fluctuating part of the DT6 pressure. However, the further load reduction to $t = 7.4$ s washes down most of the small structures, and some larger structures are formed due to a massively separated flow in the elbow region. The transient shutdown sequence finishes at $t = 8$ s, when the guide vanes stop moving, but the flow is not developed yet and needs some time to adapt to the new operating condition. Therefore, the final figure is shown at time $t = 10$ s, where the flow has reached a quasi-stationary condition. As seen in Fig. 27l, the small vortical structures are removed and only a few large ones are visible around the elbow. The new large structures are stable and remain in the draft tube and cause low-frequency high-amplitude fluctuations. The effect of such fluctuations is previously shown in the analysis of pressures and forces in the minimum load condition (for instance, Fig. 9).

The physics of the formation of rotating vortex ropes can be explained through the mechanism of Kelvin–Helmholtz instability

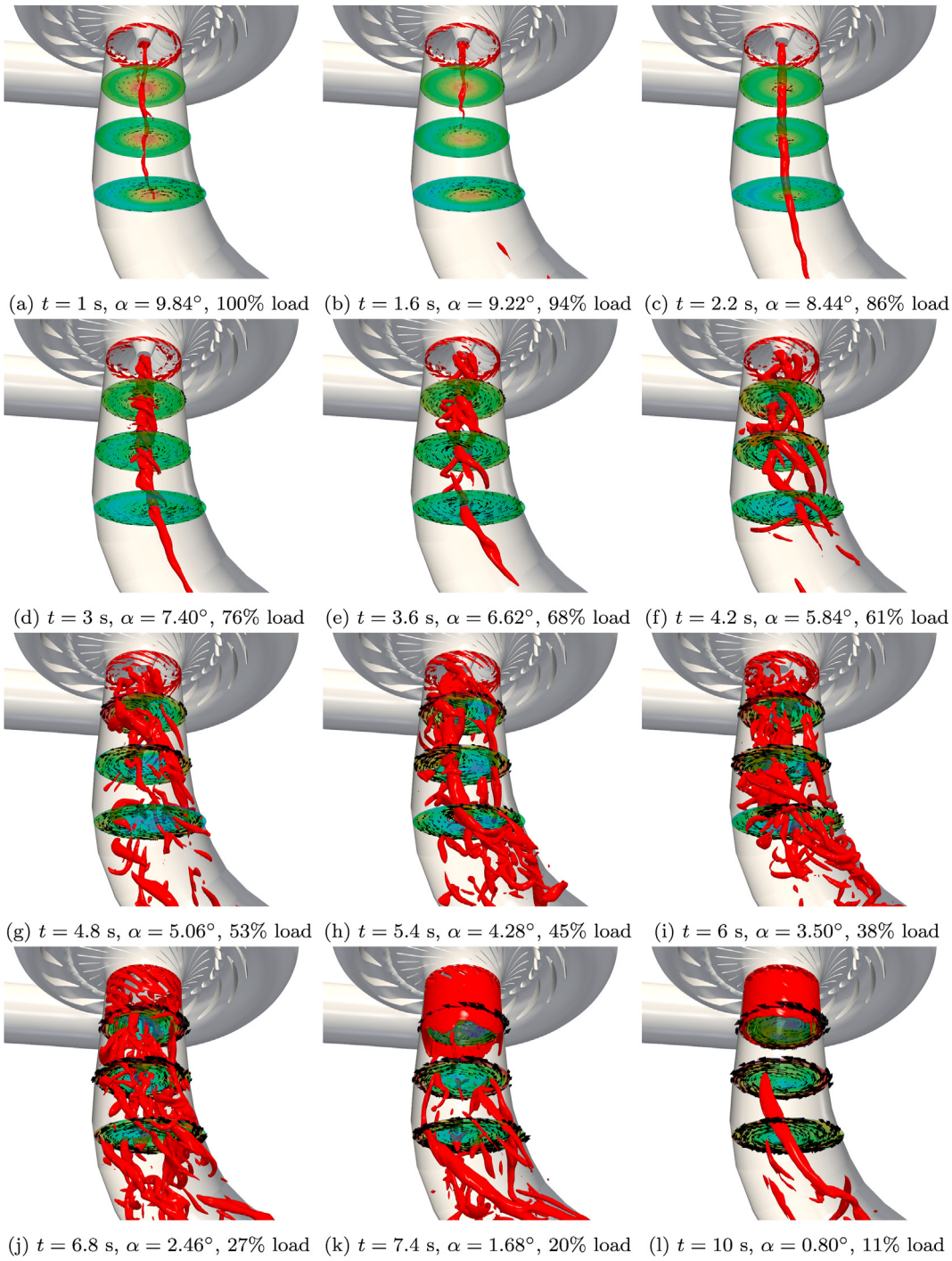

Fig. 26. Illustration of draft tube vortical structures using iso-surfaces of $\lambda_2 = 750$ s^{-2} at different times corresponding to different guide vane openings (α).

[77,78]. A stagnant region with a reversed axial flow is developed in the central region of the draft tube due to the development of a wake behind the runner cone. In addition, a highly swirling flow forms in the outer region, around the stagnant region, flowing downstream with great axial velocity. As the turbine goes deeper into the part load condition, the outer swirling flow enhances and thus the inner low-velocity region enlarges. Accordingly, sharp shear layers evolve in the draft tube at the interface of the central stagnant region and the swirling outer flow. The instability of the shear layer results in a rolling up of the interface and the creation of the rotating vortex structure. This is visualized in Fig. 27a, where both the RVR and the stagnant region are shown at $t = 4.6$ s, corresponding to a guide vane opening angle of $\alpha = 5.32°$ and a turbine load of 55.5%. The blue iso-surface of zero axial velocity ($W = 0$) reveals the stagnant region, while the RVR is shown by a red iso-surface of $\lambda_2 = 750$ s^{-2}. It is clearly seen that the RVR is formed at the interface of the stagnant and outer swirling flow regions. Thus, it is helically wrapped around the central low-velocity region. The RVR rotates around the central blue region with the approximate normalized frequency of $f/f_n \approx 0.3$. Not only does the RVR produce

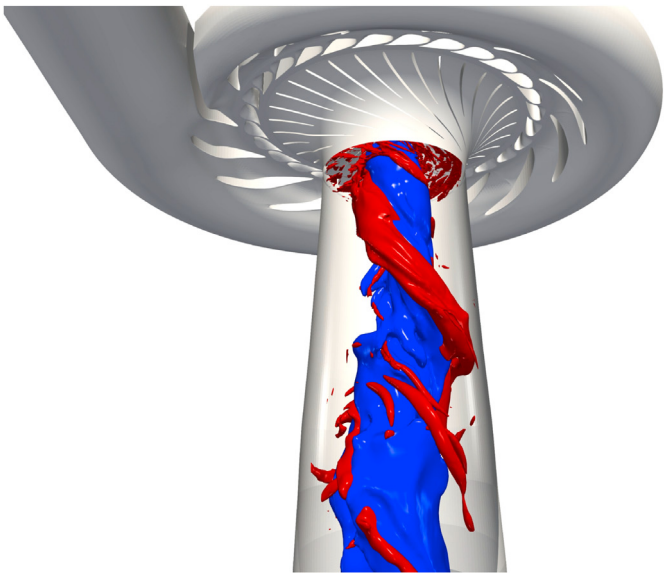

(a) $t = 4.6$ s, $\alpha = 5.32°$, 55.5% load

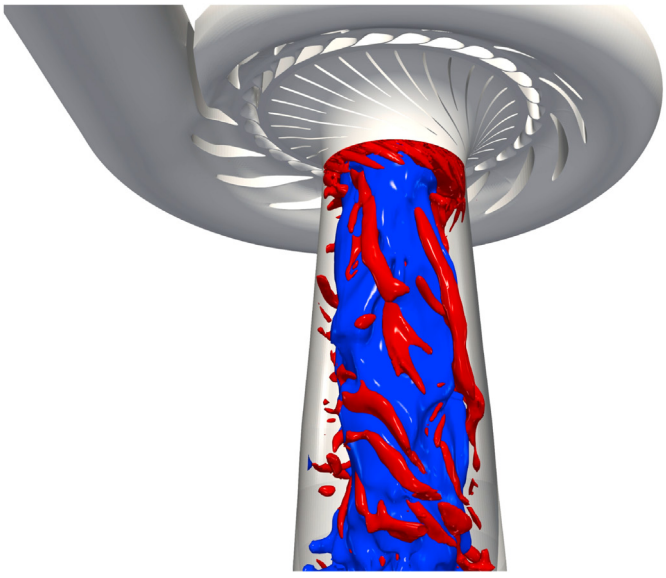

(b) $t = 6.6$ s, $\alpha = 2.72°$, 29.9% load

Fig. 27. Vortical structures (red, $\lambda_2 = 750\ s^{-2}$) and stagnant regions (blue, $W = 0$) at $t = 4.6$ and 6.6 s.

high-amplitude fluctuating forces that affect the lifetime of the turbine, but it can also increase the risk of cavitation due to the pressure drop within the vortex. As explained, the creation of a large stagnant region behind the runner cone is essential for the formation of the RVR. Thus, it is possible to reduce or remove the RVR by somehow diminishing the central wake region. Some attempts have been reported in the literature to reduce such damaging effects [79]. However, developing an efficient way of mitigation of RVR is still an open research area.

The process of the decay and disintegration of RVR can be clarified using the developing central stagnant region. Fig. 27b reveals the $\lambda_2 = 750\ s^{-2}$ (red) and $W = 0$ (blue) iso-surfaces indicating the vortical structures and stagnant region at $t = 6.6$ s, where the coherent RVR structure no longer exists. Comparing the low-velocity region to that of $t = 4.6$ s (Fig. 27a) clarifies that the stagnant region is inflating in time due to continuous growth of swirl intensity and flow rate reduction. This is also confirmed by the axial velocity contours presented in Fig. 20, where the reversed flow region is ceaselessly expanding during the shutdown sequence. As a result, the annulus space occupied by the high swirling downward outer flow region shrinks. Consequently, the RVR becomes unstable and breaks down into smaller vortical structures.

5. Conclusion

A detailed analysis of the transient flow field of a Francis turbine during a shutdown sequence was performed in this work. To the best of our knowledge, it is the first time that a comprehensive and in-depth numerical investigation is performed on a Francis turbine shutdown sequence. The computations were carried out using the OpenFOAM open-source CFD code.

The simulations were validated against experimental data at the stationary BEP condition. It was shown that the time-averaged axial velocity field in the draft tube was very well captured. A slight shift was observed between the experimental and numerical horizontal components, and a reason for that was discussed. Additionally, the turbine performance characteristics at BEP were calculated and compared to measurements to further validate the accuracy of the simulations.

The amplitude and frequency of the rotor-stator interaction pressure fluctuations in the vaneless space were accurately captured, compared to the experimental data. The blade passing frequency ($f_b = 30 f_n$) was dominant throughout the whole sequence in the vaneless space, while the low-frequency oscillations generated by the flow structures in the draft tube dominate the pressure fluctuations of the draft tube pressure probes. Low-frequency high-amplitude pulsations caused by the formation of the RVR started at around $t = 4$ s and decayed after $t = 6$ s due to the collapse of the vortex rope. At the minimum load condition, a wide range of stochastic frequencies was observed in both the vaneless space and the draft tube, which was described through the guide vane vortex shedding and the breakdown of small vortical structures in the draft tube. A signal coherence study revealed that the low-frequency pressure fluctuations due to flow structures, such as RVR, are out-of-phase for two probes located at opposite sides in the draft tube.

The axial force exerted on the runner, which is initially upward, decreases and changes direction. Both the axial and horizontal forces exhibit remarkable pulsations at part load with the creation of the RVR. At the minimum load condition, the pulsations of the horizontal force are significantly smaller than the part load, while axial force still shows large pulsations. The axial force fluctuations are more chaotic than the horizontal ones, and its spectrogram shows a range of excited stochastic frequencies, whereas the horizontal force mostly fluctuates with deterministic frequencies.

The time-variation of the axial velocity field in the draft tube indicates the development of a reversed flow region around the center. All three velocity components showed large oscillation due to the formation of the RVR between $t = 4$ s and $t = 6$ s. The velocity component normal to the experimental PIV plane revealed a weak counter-rotating swirl at BEP. As the flow rate decreases, the normal velocity component becomes momentarily zero, and then a positive swirl forms and intensifies.

The λ_2-criterion was employed to describe the flow structures in the draft tube. The physical phenomena behind the formation and collapse of the RVR were explained in detail. A slender vortex rope was present at BEP and vanished after a short while into the transient sequence and then another stationary vortex rope establishes at the center. It becomes unstable and complex rotating vortical structures are created from the runner hub. Later, some of these vortical structures are merged together and create one large rotating structure, i.e. the RVR. The central stagnant region inflates

in time and makes the RVR unstable, resulting in its disintegration into smaller structures. At the minimum load, the small vortical structures are washed away and only a few large ones remain near the elbow.

CRediT authorship contribution statement

Saeed Salehi: Conceptualization, Methodology, Software, Investigation, Writing – review & editing. **Håkan Nilsson:** Conceptualization, Supervision, Writing – review & editing, Funding acquisition. **Eric Lillberg:** Writing – review & editing. **Nicolas Edh:** Writing – review & editing.

Declaration of competing interest

The authors declare that they have no known competing financial interests or personal relationships that could have appeared to influence the work reported in this paper.

Acknowledgements

The current research was carried out as a part of the "Swedish Hydropower Centre - SVC". SVC is established by the Swedish Energy Agency, EnergiForsk and Svenska Kraftnät together with Luleå University of Technology, The Royal Institute of Technology, Chalmers University of Technology and Uppsala University, www.svc.nu.

The computations were enabled by resources provided by the Swedish National Infrastructure for Computing (SNIC) at NSC and C3SE partially funded by the Swedish Research Council through grant agreement no. 2018–05973.

The investigated test case is provided by NTNU – Norwegian University of Science and Technology under the Francis-99 workshop series.

References

[1] REN21, Renewables 2015 global status report, (Paris: REN21 Secretariat), URL, https://www.ren21.net/wp-content/uploads/2019/05/GSR2015_Full-Report_English.pdf, 2015.
[2] REN21, Renewables 2020 Global Status Report, (Paris: REN21 Secretariat), URL, https://www.ren21.net/wp-content/uploads/2019/05/gsr_2020_full_report_en.pdf, 2020.
[3] R. Goyal, B.K. Gandhi, Review of hydrodynamics instabilities in Francis turbine during off-design and transient operations, Renew. Energy 116 (2018) 697–709, https://doi.org/10.1016/j.renene.2017.10.012.
[4] P. Sorknæs, A.N. Andersen, J. Tang, S. Strøm, Market integration of wind power in electricity system balancing, Energy Strategy Reviews 1 (3) (2013) 174–180, https://doi.org/10.1016/j.esr.2013.01.006, future Energy Systems and Market Integration of Wind Power.
[5] C. Trivedi, E. Agnalt, O.G. Dahlhaug, Investigations of unsteady pressure loading in a Francis turbine during variable-speed operation, Renew. Energy 113 (2017) 397–410, https://doi.org/10.1016/j.renene.2017.06.005.
[6] G. Caralis, D. Papantonis, A. Zervos, The role of pumped storage systems towards the large scale wind integration in the Greek power supply system, Renew. Sustain. Energy Rev. 16 (5) (2012) 2558–2565, https://doi.org/10.1016/j.rser.2012.01.068.
[7] J. Hell, High flexible hydropower generation concepts for future grids, J. Phys. Conf. 813 (2017), https://doi.org/10.1088/1742-6596/813/1/012007, 012007.
[8] C. Trivedi, B. Gandhi, C.J. Michel, Effect of transients on Francis turbine runner life: a review, J. Hydraul. Res. 51 (2) (2013) 121–132, https://doi.org/10.1080/00221686.2012.732971.
[9] H.-J. Huth, Fatigue design of hydraulic turbine runners, Ph.D. thesis, Norwegian University of Science and Technology (NTNU), 2005.
[10] C. Deschênes, R. Fraser, J.-P. Fau, New trends in turbine modelling and new ways of partnership, in: International Conference on Hydraulic Efficiency Measurement—IGHEM, Toronto, Ontario, Canada, July, 2002, pp. 17–19.
[11] C. Nicolet, Hydroacoustic modelling and numerical simulation of unsteady operation of hydroelectric systems, Ph.D. thesis, École Polytechnique Fédérale de Lausanne (EPFL), 2007.
[12] C. Trivedi, M.J. Cervantes, B. Gandhi, O.G. Dahlhaug, Pressure measurements on a high-head Francis turbine during load acceptance and rejection, J. Hydraul. Res. 52 (2) (2014) 283–297, https://doi.org/10.1080/00221686.2013.854846.
[13] R. Goyal, M.J. Cervantes, B.K. Gandhi, Vortex rope formation in a high head model Francis turbine, J. Fluid Eng. 139 (4) (02 2017), https://doi.org/10.1115/1.4035224, 041102.
[14] N. Sotoudeh, R. Maddahian, M.J. Cervantes, Investigation of rotating vortex rope formation during load variation in a Francis turbine draft tube, Renew. Energy 151 (2020) 238–254, https://doi.org/10.1016/j.renene.2019.11.014.
[15] S. Salehi, H. Nilsson, E. Lillberg, N. Edh, Development of a novel numerical framework in OpenFOAM to simulate kaplan turbine transients, IOP Conf. Ser. Earth Environ. Sci. 774 (1) (2021), https://doi.org/10.1088/1755-1315/774/1/012058, 012058.
[16] M. Gagnon, S.A. Tahan, P. Bocher, D. Thibault, Impact of startup scheme on Francis runner life expectancy, in: IOP Conference Series: Earth and Environmental Science, vol. 12, 2010, https://doi.org/10.1088/1755-1315/12/1/012107, 012107.
[17] M. Gagnon, J. Nicolle, J.-F. Morissette, M. Lawrence, A look at Francis runner blades response during transients, in: IOP Conference Series: Earth and Environmental Science, vol. 49, 2016, https://doi.org/10.1088/1755-1315/49/5/052005, 052005.
[18] C. Trivedi, M.J. Cervantes, B.K. Gandhi, O.G. Dahlhaug, Experimental investigations of transient pressure variations in a high head model Francis turbine during start-up and shutdown, Journal of Hydrodynamics, Ser B 26 (2) (2014) 277–290, https://doi.org/10.1016/S1001-6058(14)60031-7.
[19] C. Trivedi, B.K. Gandhi, M.J. Cervantes, O.G. Dahlhaug, Experimental investigations of a model Francis turbine during shutdown at synchronous speed, Renew. Energy 83 (2015) 828–836, https://doi.org/10.1016/j.renene.2015.05.026.
[20] J. Unterluggauer, V. Sulzgruber, E. Doujak, C. Bauer, Experimental and numerical study of a prototype Francis turbine startup, Renew. Energy 157 (2020) 1212–1221, https://doi.org/10.1016/j.renene.2020.04.156.
[21] J. Nicolle, J.F. Morissette, A.M. Giroux, Transient CFD simulation of a Francis turbine startup, IOP Conf. Ser. Earth Environ. Sci. 15 (6) (2012), https://doi.org/10.1088/1755-1315/15/6/062014, 062014.
[22] Z. Li, H. Bi, B. Karney, Z. Wang, Z. Yao, Three-dimensional transient simulation of a prototype pump-turbine during normal turbine shutdown, J. Hydraul. Res. 55 (4) (2017) 520–537, https://doi.org/10.1080/00221686.2016.1276105.
[23] J. Fahlbeck, H. Nilsson, S. Salehi, M. Zangeneh, M. Joseph, Numerical analysis of an initial design of a counter-rotating pump-turbine, IOP Conf. Ser. Earth Environ. Sci. 774 (1) (2021), https://doi.org/10.1088/1755-1315/774/1/012066, 012066.
[24] J. Fahlbeck, H. Nilsson, S. Salehi, Flow characteristics of preliminary shutdown and startup sequences for a model counter-rotating pump-turbine, Energies 14 (12) (2021), https://doi.org/10.3390/en14123593.
[25] T. Kolšek, J. Duhovnik, A. Bergant, Simulation of unsteady flow and runner rotation during shut-down of an axial water turbine, J. Hydraul. Res. 44 (1) (2006) 129–137, https://doi.org/10.1080/00221686.2006.9521668.
[26] P. Mössinger, R. Jester-Zürker, A. Jung, Francis-99: transient CFD simulation of load changes and turbine shutdown in a model sized high-head Francis turbine, J. Phys. Conf. 782 (2017), https://doi.org/10.1088/1742-6596/782/1/012001, 012001.
[27] S. Salehi, H. Nilsson, E. Lillberg, N. Edh, Numerical simulation of hydraulic turbine during transient operation using OpenFOAM, IOP Conf. Ser. Earth Environ. Sci. 774 (1) (2021), https://doi.org/10.1088/1755-1315/774/1/012060, 012060.
[28] C. Trivedi, M.J. Cervantes, B.K. Gandhi, O.G. Dahlhaug, Experimental and numerical studies for a high head Francis turbine at several operating points, J. Fluid Eng. 135 (11) (08 2013), https://doi.org/10.1115/1.4024805, 111102.
[29] Francis-99, https://www.ntnu.edu/nvks/francis-99, accessed: 2020-01-28 (2020).
[30] F. Menter, Y. Egorov, A scale adaptive simulation model using two-equation models, in: 43rd AIAA Aerospace Sciences Meeting and Exhibit, 2005, p. 1095, https://doi.org/10.2514/6.2005-1095.
[31] Y. Egorov, F. Menter, Development and application of SST-SAS turbulence model in the DESIDER project, in: S.-H. Peng, W. Haase (Eds.), Advances in Hybrid RANS-LES Modelling, Springer Berlin Heidelberg, Berlin, Heidelberg, 2008, pp. 261–270, https://doi.org/10.1007/978-3-540-77815-8_27.
[32] F.R. Menter, Two-equation eddy-viscosity turbulence models for engineering applications, AIAA Journal 32(8) (1994) 1598–1605, https://doi.org/10.2514/3.12149.
[33] F.R. Menter, Y. Egorov, SAS turbulence modelling of technical flows, in: E. Lamballais, R. Friedrich, B.J. Geurts, O. Métais (Eds.), Direct and Large-Eddy Simulation VI, Springer Netherlands, Dordrecht, 2006, pp. 687–694, https://doi.org/10.1007/978-1-4020-5152-2_79.
[34] M. Younsi, A. Djerrada, T. Belamri, F. Menter, Application of the SAS turbulence model to predict the unsteady flow field behaviour in a forward centrifugal fan, Int. J. Comput. Fluid Dynam. 22 (9) (2008) 639–648, https://doi.org/10.1080/10618560802432944.
[35] F.R. Menter, Review of the shear-stress transport turbulence model experience from an industrial perspective, Int. J. Comput. Fluid Dynam. 23 (4) (2009) 305–316, https://doi.org/10.1080/10618560902773387.
[36] F. Menter, Y. Egorov, The scale-adaptive simulation method for unsteady turbulent flow predictions. part 1: theory and model description, Flow, Turbul. Combust. 85 (1) (2010) 113–138, https://doi.org/10.1007/s10494-010-9264-5.
[37] Y. Egorov, F. Menter, R. Lechner, D. Cokljat, The scale-adaptive simulation

method for unsteady turbulent flow predictions. part 2: application to complex flows, Flow, Turbul. Combust. 85 (1) (2010) 139–165, https://doi.org/10.1007/s10494-010-9265-4.
[38] F. Menter, J. Schutze, K. Kurbatskii, R. Lechner, M. Gritskevich, A. Garbaruk, Scale-resolving simulation techniques in industrial CFD, in: 6th AIAA Theoretical Fluid Mechanics Conference, 2011, p. 3474, https://doi.org/10.2514/6.2011-3474.
[39] V. Hasmatuchi, Hydrodynamics of a pump-turbine operating at off-design conditions in generating mode, Ph.D. thesis, EPFL, 2012.
[40] T. Krappel, A. Ruprecht, S. Riedelbauch, R. Jester-Zuerker, A. Jung, Investigation of Francis turbine part load instabilities using flow simulations with a hybrid RANS-LES turbulence model, IOP Conf. Ser. Earth Environ. Sci. 22 (3) (2014), https://doi.org/10.1088/1755-1315/22/3/032001, 032001.
[41] A. Javadi, H. Nilsson, A comparative study of scale-adaptive and large-eddy simulations of highly swirling turbulent flow through an abrupt expansion, IOP Conf. Ser. Earth Environ. Sci. 22 (2) (2014), https://doi.org/10.1088/1755-1315/22/2/022017, 022017.
[42] J. Nicolle, S. Cupillard, Prediction of dynamic blade loading of the Francis-99 turbine, J. Phys. Conf. 579 (2015), https://doi.org/10.1088/1742-6596/579/1/012001, 012001.
[43] C. Trivedi, Investigations of compressible turbulent flow in a high-head Francis turbine, J. Fluid Eng. 140 (1) (09 2017), https://doi.org/10.1115/1.4037500, 011101.
[44] C. Trivedi, A systematic validation of a Francis turbine under design and off-design loads, Journal of Verification, Validation and Uncertainty Quantification 4 (1) (06 2019), https://doi.org/10.1115/1.4043965, 011003.
[45] J. Decaix, V. Hasmatuchi, M. Titzschkau, C. Münch-Alligné, CFD investigation of a high head Francis turbine at speed no-load using advanced urans models, Appl. Sci. 8 (12) (2018) 2505, https://doi.org/10.3390/app8122505.
[46] OpenCFD, OpenFOAM - the Open Source CFD Toolbox - User's Guide, 2019. Version v1912, OpenCFD Ltd.
[47] H.G. Weller, G. Tabor, H. Jasak, C. Fureby, A tensorial approach to computational continuum mechanics using object-oriented techniques, Comput. Phys. 12 (6) (1998), https://doi.org/10.1063/1.168744, 620–.
[48] H. Jasak, Error analysis and estimation for the finite volume method with applications to fluid flows, Ph.D. thesis, Imperial College London, 1996.
[49] R. Courant, K. Friedrichs, H. Lewy, Über die partiellen differenzengleichungen der mathematischen physik, Math. Ann. 100 (1) (1928) 32–74, https://doi.org/10.1007/BF01448839.
[50] H. Weller, Controlling the computational modes of the arbitrarily structured C grid, Mon. Weather Rev. 140 (10) (2012) 3220–3234, https://doi.org/10.1175/MWR-D-11-00221.1.
[51] S. Patankar, D. Spalding, A calculation procedure for heat, mass and momentum transfer in three-dimensional parabolic flows, Int. J. Heat Mass Tran. 15 (10) (1972) 1787–1806, https://doi.org/10.1016/0017-9310(72)90054-3.
[52] R. Issa, Solution of the implicitly discretised fluid flow equations by operator-splitting, J. Comput. Phys. 62 (1) (1986) 40–65, https://doi.org/10.1016/0021-9991(86)90099-9.
[53] E. Robertson, V. Choudhury, S. Bhushan, D. Walters, Validation of OpenFOAM numerical methods and turbulence models for incompressible bluff body flows, Comput. Fluids 123 (2015) 122–145, https://doi.org/10.1016/j.compfluid.2015.09.010.
[54] T. Holzmann, Mathematics, Numerics, Derivations and OpenFOAM®, seventh ed., 2019, https://doi.org/10.13140/RG.2.2.27193.36960. Holzmann CFD.
[55] C.M. Rhie, W.L. Chow, Numerical study of the turbulent flow past an airfoil with trailing edge separation, AIAA J. 21 (11) (1983) 1525–1532, https://doi.org/10.2514/3.8284.
[56] F.P. Kärrholm, Numerical Modelling of Diesel Spray Injection, Turbulence Interaction and Combustion, Ph.D. thesis, Chalmers University of Technology Gothenburg, Sweden, 2008.
[57] J.H. Ferziger, M. Perić, R.L. Street, Computational Methods for Fluid Dynamics, vol. 3, Springer, 2002, https://doi.org/10.1007/978-3-642-56026-2.
[58] W. Zeng, J. Yang, J. Hu, J. Yang, Guide-vane closing schemes for pump-turbines based on transient characteristics in S-shaped region, J. Fluid Eng. 138 (5) (01 2016), https://doi.org/10.1115/1.4032069, 051302.
[59] Y. Dewan, C. Custer, A. Ivashchenko, Simulation of the Francis-99 hydro turbine during steady and transient operation, J. Phys. Conf. 782 (2017), https://doi.org/10.1088/1742-6596/782/1/012003, 012003.
[60] C. Trivedi, Time-dependent inception of vortex rings in a Francis turbine during load variation: large eddy simulation and experimental validation, J. Hydraul. Res. 58 (5) (2020) 790–806, https://doi.org/10.1080/00221686.2019.1671514.
[61] K.-R.G. Jakobsen, M.A. Holst, CFD simulations of transient load change on a high head francis turbine, J. Phys. Conf. 782 (2017), https://doi.org/10.1088/1742-6596/782/1/012002, 012002.
[62] P. Farrell, J. Maddison, Conservative interpolation between volume meshes by local galerkin projection, Comput. Methods Appl. Mech. Eng. 200 (1) (2011) 89–100, https://doi.org/10.1016/j.cma.2010.07.015.
[63] H.J. Aguerre, S. Márquez Damián, J.M. Gimenez, N.M. Nigro, Conservative handling of arbitrary non-conformal interfaces using an efficient supermesh, J. Comput. Phys. 335 (2017) 21–49, https://doi.org/10.1016/j.jcp.2017.01.018.
[64] F. Pellegrini, J. Roman, Scotch: a software package for static mapping by dual recursive bipartitioning of process and architecture graphs, in: H. Liddell, A. Colbrook, B. Hertzberger, P. Sloot (Eds.), High-Performance Computing and Networking, Springer Berlin Heidelberg, Berlin, Heidelberg, 1996, pp. 493–498, https://doi.org/10.1007/3-540-61142-8_588.
[65] W. Gropp, W.D. Gropp, E. Lusk, A. Skjellum, A.D.F.E.E. Lusk, Using MPI: portable parallel programming with the message-passing interface, 1, MIT press, 1999. https://mitpress.mit.edu/books/using-mpi-third-edition.
[66] H. Jasak, Z. Tuković, Automatic mesh motion for the unstructured finite volume method, Transactions of FAMENA 30 (2) (2006) 1–20.
[67] H. Jasak, Dynamic mesh handling in OpenFOAM, in: 47th AIAA Aerospace Sciences Meeting Including the New Horizons Forum and Aerospace Exposition, 2009, p. 341, https://doi.org/10.2514/6.2009-341.
[68] F.M. Bos, Numerical simulations of flapping foil and wing aerodynamics: mesh deformation using radial basis functions, Ph.D. thesis, TU Delft, 2010.
[69] A. Savitzky, M.J.E. Golay, Smoothing and differentiation of data by simplified least squares procedures, Anal. Chem. 36 (8) (1964) 1627–1639, https://doi.org/10.1021/ac60214a047.
[70] B. Nennemann, J.F. Morissette, J. Chamberland-Lauzon, C. Monette, O. Braun, M. Melot, A. Coutu, J. Nicolle, A.M. Giroux, Challenges in dynamic pressure and stress predictions at no-load operation in hydraulic turbines, IOP Conf. Ser. Earth Environ. Sci. 22 (3) (2014), https://doi.org/10.1088/1755-1315/22/3/032055, 032055.
[71] J. Morissette, J. Chamberland-Lauzon, B. Nennemann, C. Monette, A. Giroux, A. Coutu, J. Nicolle, Stress predictions in a Francis turbine at no-load operating regime, IOP Conf. Ser. Earth Environ. Sci. 49 (2016), https://doi.org/10.1088/1755-1315/49/7/072016, 072016.
[72] Z.M. Hussain, A.Z. Sadik, P. O'Shea, Digital signal processing: an introduction with MATLAB and applications, Springer Science & Business Media, 2011, https://doi.org/10.1007/978-3-642-15591-8.
[73] P. Dörfler, M. Sick, A. Coutu, Flow-induced pulsation and vibration in hydroelectric machinery: engineer's guidebook for planning, design and troubleshooting, Springer-Verlag London, 2013, https://doi.org/10.1007/978-1-4471-4252-2.
[74] W. Gyllenram, Analytical and numerical studies of internal swirling flows, Ph.D. thesis, Chalmers University of Technology, 2008.
[75] Y. Zhang, K. Liu, H. Xian, X. Du, A review of methods for vortex identification in hydroturbines, Renew. Sustain. Energy Rev. 81 (2018) 1269–1285, https://doi.org/10.1016/j.rser.2017.05.058.
[76] J. Jeong, F. Hussain, On the identification of a vortex, J. Fluid Mech. 285 (1995) 69–94, https://doi.org/10.1017/S0022112095000462.
[77] H. Foroutan, S. Yavuzkurt, Flow in the simplified draft tube of a Francis turbine operating at partial load—Part I: simulation of the vortex rope, J. Appl. Mech. 81 (6) (03 2014), https://doi.org/10.1115/1.4026817, 061010.
[78] R. Goyal, B.K. Gandhi, M.J. Cervantes, Experimental study of mitigation of a spiral vortex breakdown at high Reynolds number under an adverse pressure gradient, Phys. Fluids 29 (10) (2017) 104104, https://doi.org/10.1063/1.4999123.
[79] S. Kumar, M.J. Cervantes, B.K. Gandhi, Rotating vortex rope formation and mitigation in draft tube of hydro turbines – a review from experimental perspective, Renew. Sustain. Energy Rev. 136 (2021) 110354, https://doi.org/10.1016/j.rser.2020.110354.